

1 The rupture extent of low frequency earthquakes near Parkfield, CA

2 Jessica C. Hawthorne (Department of Earth Sciences, University of Oxford, Oxford, UK)

3 Amanda M. Thomas (Department of Earth Sciences, University of Oregon, Oregon, USA)

4 Jean-Paul Ampuero (Université Côte d'Azur, IRD, CNRS, Observatoire de la Côte d'Azur, France;
5 California Institute of Technology, Seismological Laboratory, Divisional of Geological and Planetary
6 Sciences, Pasadena, CA, USA)

7 Manuscript submitted to *Geophysical Journal International*

8 **Abstract**

9 The low frequency earthquakes (LFEs) that constitute tectonic tremor are often inferred to
10 be slow: to have durations of 0.2 to 0.5 s, a factor of 10 to 100 longer than those of typical
11 M_W 1-2 earthquakes. Here we examine LFEs near Parkfield, CA in order to assess several
12 proposed explanations for LFEs' long durations. We determine LFE rupture areas and loca-
13 tion distributions using a new approach, similar to directivity analysis, where we examine how
14 signals coming from various locations within LFEs' finite rupture extents create differences in
15 the apparent source time functions recorded at various stations. We use synthetic ruptures to
16 determine how much the LFE signals recorded at each station would be modified by spatial
17 variations of the source-station travel time within the rupture area given various possible rup-
18 ture diameters, and then compare those synthetics with the data. Our synthetics show that the
19 methodology can identify inter-station variations created by heterogeneous slip distributions or
20 complex rupture edges, and thus lets us estimate LFE rupture extents for unilateral or bilateral
21 ruptures. To obtain robust estimates of the sources' similarity across stations, we stack signals
22 from thousands of LFEs, using an empirical Green's function approach to isolate the LFEs'
23 apparent source time functions from the path effects. Our analysis of LFEs in Parkfield implies
24 that LFEs' apparent source time functions are similar across stations at frequencies up to 8 to
25 16 Hz, depending on the family.

26 The inter-station coherence observed at these relatively high frequencies, or short wave-
27 lengths (down to 0.2 to 0.5 km), suggest that LFEs in each of the 7 families examined occur on
28 asperities. They are clustered in patches with sub-1-km diameters. The individual LFEs' rup-
29 ture diameters are estimated to be smaller than 1.1 km for all families, and smaller than 0.5 km
30 and 1 km for the two shallowest families, which were previously found to have 0.2-s durations.
31 Coupling the diameters with the durations suggests that it is possible to model these M_W 1-2
32 LFEs with earthquake-like rupture speeds: around 70% of the shear wave speed. However,
33 that rupture speed matches the data only at the edge of our uncertainty estimates for the family
34 with highest coherence. The data for that family are better matched if LFEs have rupture ve-
35 locities smaller than 40% of the shear wave speed, or if LFEs have different rupture dynamics.
36 They could have long rise times, contain composite sub-ruptures, or have slip distributions that
37 persist from event to event.

38 1 Introduction

39 Tectonic tremor is a long-duration seismic signal, best observed at frequencies between 1 and 10 Hz
40 (e.g., *Obara*, 2002; *Rogers and Dragert*, 2003; *Payero et al.*, 2008; *Peterson and Christensen*,
41 2009; *Rubinstein et al.*, 2009; *Fry et al.*, 2011). It is thought to consist of numerous small low
42 frequency earthquakes, or LFEs (*Shelly et al.*, 2006, 2007; *Wech and Creager*, 2007; *Brown et al.*,
43 2009). LFEs are often inferred to have magnitudes between M_W 1 and 2.5 but to have corner
44 frequencies of a few Hz, a factor of 10 to 100 times smaller than corner frequencies observed for
45 “normal” M_W 1-2.5 earthquakes (*Fletcher and McGarr*, 2011; *Zhang et al.*, 2011; *Bostock et al.*,
46 2017). LFEs are found to have durations around 0.2 seconds in Parkfield (*Thomas et al.*, 2016)
47 and around 0.5 s in Cascadia (*Bostock et al.*, 2015), which are a factor of 10 to 100 longer than
48 “normal” M_W 1-2.5 earthquakes.

49 1.1 Potential Causes of LFEs’ Long Durations

50 The durations of typical earthquakes are determined by their spatial extent: by how long it takes the
51 rupture to progress across the earthquake area. Models and observations suggest that earthquake
52 ruptures usually progress at speeds of 2 to 3 km/s, or 60 to 95% of the shear wave speed V_s
53 (*Kanamori and Brodsky*, 2004; *McGuire*, 2004; *Madariaga*, 2007; *Seekins and Boatwright*, 2010;
54 *Taira et al.*, 2015; *Folesky et al.*, 2016; *Ye et al.*, 2016; *Melgar and Hayes*, 2017; *Chouvet et al.*,
55 2018). Earthquakes’ durations can thus be roughly estimated by dividing their rupture lengths
56 by the shear wave speed. If LFEs, like normal earthquakes, rupture at speeds close to the shear
57 wave speed, their long durations could indicate that LFEs have unusually large lengths given their
58 moment: perhaps 0.7 to 1.5 km. In this scenario, LFEs would have lower stress drops than normal
59 earthquakes—0.1 to 10 kPa, but they could otherwise be governed by the same physical processes.
60 LFEs could be driven by unstable frictional sliding, and their slip speeds could be limited by the
61 energy that they dissipate via seismic waves (e.g., *Rice*, 1980; *Kanamori and Brodsky*, 2004).

62 However, it is also possible that seismic wave generation has minimal impact on LFE dynamics,
63 and that LFEs are governed by different fault zone processes. LFEs’ slip rates may be limited by
64 a spatial constraint or by a speed-limiting frictional rheology (e.g., *Liu and Rice*, 2005, 2007;
65 *Shibazaki and Shimamoto*, 2007; *Rubin*, 2008; *Segall et al.*, 2010; *Skarbek et al.*, 2012; *Fagereng*
66 *et al.*, 2014; *Yabe and Ide*, 2017). For instance, LFEs might occur on faults with a velocity-
67 strengthening rheology, which inhibits increases in slip rate. The brief slip rate increases seen in
68 LFEs could result from imposed local stress concentrations, perhaps created by the creep fronts of
69 large slow slip events (e.g., *Perfettini and Ampuero*, 2008; *Rubin*, 2009). Alternatively, LFEs could
70 occur on faults with a more complex rheology, which encourages initial increases in slip rate but
71 inhibits slip rates higher than some cutoff speed. Such rheologies are commonly proposed for slow
72 slip events and may be created by shear-induced dilatancy or by a minimum asperity size (e.g.,
73 *Shibazaki and Iio*, 2003; *Shibazaki and Shimamoto*, 2007; *Liu et al.*, 2010; *Segall et al.*, 2010;
74 *Hawthorne and Rubin*, 2013; *Poulet et al.*, 2014). The possibility that LFEs are small versions of
75 slow slip events is intriguing because slip rates vary widely from slow slip to tremor (*Ide et al.*,
76 2007, 2008; *Aguiar et al.*, 2009; *Gao et al.*, 2012; *Ide and Yabe*, 2014; *Hawthorne and Bartlow*,
77 2018). Several of the processes proposed to govern slow slip would have difficulty producing
78 such a wide range of slip rates (e.g., *Liu and Rice*, 2005, 2007; *Shibazaki and Shimamoto*, 2007;
79 *Hawthorne and Rubin*, 2013; *Fagereng et al.*, 2014; *Veveakis et al.*, 2014). If LFE slip rates are

80 limited primarily by frictional resistance to shear and not by seismic wave radiation, LFEs need not
81 rupture across the fault at speeds close to the shear wave speed. They could rupture more slowly
82 and have diameters far smaller than 1 km despite their 0.2-s durations.

83 LFEs could also have small rupture diameters if their 0.2-s durations and low corner frequencies
84 are actually apparent values, not true ones. LFEs could be “normal” M_W 1-2.5 earthquakes, with
85 0.01-s durations and 10-m rupture diameters. They may appear to be dominated by low-frequency
86 signals only because their high-frequency signals are attenuated when they pass through a highly
87 damaged fault zone or through a region of high pore fluid pressure (Gomberg *et al.*, 2012; Bostock
88 *et al.*, 2017). Regions of high pore pressure or increased attenuation are frequently identified near
89 the slow slip region (Audet *et al.*, 2009; Song *et al.*, 2009; van Avendonk *et al.*, 2010; Kato *et al.*,
90 2010; Fagereng and Diener, 2011; Kitajima and Saffer, 2012; Nowack and Bostock, 2013; Yabe
91 *et al.*, 2014; Saffer and Wallace, 2015; Audet and Schaeffer, 2018), though we note that any regions
92 with attenuation strong enough to produce tremor’s frequency content might have to be localized
93 into patches. Earthquakes do occur below the tremor-generating region, and some of them show
94 higher-frequency signals than tremor (Seno and Yamasaki, 2003; Shelly *et al.*, 2006; Bell *et al.*,
95 2010; Kato *et al.*, 2010; Gomberg *et al.*, 2012; Bostock *et al.*, 2017).

96 1.2 Potential Role of Tremor Asperities

97 Tremor is often patchily distributed along the plate interface; it is densely concentrated in some
98 regions but appears absent in others (e.g., Payero *et al.*, 2008; Maeda and Obara, 2009; Walter
99 *et al.*, 2011; Ghosh *et al.*, 2012; Armbruster *et al.*, 2014). Some observations and models suggest
100 that tremor occurs only on a set of tremor-generating asperities (e.g., Ariyoshi *et al.*, 2009; Ando
101 *et al.*, 2010; Shelly, 2010b; Nakata *et al.*, 2011; Ando *et al.*, 2012; Sweet *et al.*, 2014; Veedu and
102 Barbot, 2016; Chestler and Creager, 2017a,b; Luo and Ampuero, 2017). Such asperities may also
103 be suggested by the success of template matching approaches to tremor identification, in which
104 LFEs are detected and grouped into families according to waveform similarity. Each LFE family
105 could reflect an individual tremor asperity (Shelly *et al.*, 2007; Brown *et al.*, 2008; Bostock *et al.*,
106 2012; Frank *et al.*, 2013; Kato, 2017; Shelly, 2017). However, the family grouping could also result
107 from more gradual variations in the path effects. LFEs located more than 1 or a few km away from
108 each other may be grouped into distinct families simply because the path effects vary significantly
109 on several-km length scales, so that well-separated LFEs give rise to distinct seismograms.

110 A few studies have provided further indications that LFE families reflect tremor clusters. Sweet
111 *et al.* (2014) relocated LFEs within an isolated family in Cascadia and found that they clustered
112 within a 1-km-wide patch. Chestler and Creager (2017b) relocated LFEs within around 20 families
113 in Cascadia and found that LFEs cluster within 1 to 2-km-wide patches that are often separated by
114 > 5-km-wide areas with few to no LFEs. Tremor-generating asperities are also suggested by the
115 highly repetitive recurrence intervals of one isolated LFE family near Parkfield, CA, which suggest
116 that the LFEs could be repeating similar ruptures of a particular asperity (Shelly, 2010b; Veedu and
117 Barbot, 2016). Repetitive LFE rupture is also suggested by LFE moments and durations that vary
118 little from event to event, creating exponential amplitude distributions (Watanabe *et al.*, 2007;
119 Shelly and Hardebeck, 2010; Chamberlain *et al.*, 2014; Sweet *et al.*, 2014; Bostock *et al.*, 2015;
120 Chestler and Creager, 2017a), though it is also possible that each LFE ruptures only a portion of a
121 tremor-generating asperity. The total slip on an LFE patch could result from a range of ruptures of
122 different types, as well as some aseismic slip (Chestler and Creager, 2017a).

123 **1.3 Analysis to Be Presented**

124 In this study, we further assess whether small asperities control tremor generation and whether
125 LFEs are governed by earthquake-like or slow slip rheologies by determining the rupture extents
126 of LFEs in seven families near Parkfield, CA. We will place upper bounds on the spatial distribution
127 of LFEs in each family and on the average LFE rupture area. In order to obtain these bounds, we
128 will introduce a new coherence-based approach, which can be thought of as a version of directivity
129 analysis that we have modified so that we can combine data from thousands of LFEs which may
130 rupture unilaterally or bilaterally (e.g. *Mueller*, 1985; *Mori and Frankel*, 1990; *Got and Fréchet*,
131 1993; *Velasco et al.*, 1994; *Lengliné and Got*, 2011; *Wang and Rubin*, 2011; *Kane et al.*, 2013). We
132 examine how signals coming from various locations within LFEs' finite rupture areas can produce
133 complex apparent source time functions (ASTFs) that vary from station to station. We quantify the
134 ASTF variation as a function of frequency, or seismic wavelength, in order to determine the LFE
135 rupture area.

136 We qualitatively explain how the ASTFs' frequency-dependent variability should reflect LFEs'
137 rupture extents in section 2. In section 3, we present our approach in more detail. We describe
138 how we can isolate the ASTFs from observed seismograms using an empirical Green's function
139 approach and then how we can quantify the ASTFs' coherence among LFEs and among stations. In
140 sections 4 and 5, we analyze ASTF coherence for individual LFEs near Parkfield and then average
141 over thousands of LFEs to obtain well-resolved estimates of inter-station coherence as a function
142 of frequency. For comparison, we also compute ASTF coherence for a suite of synthetic LFEs with
143 a range of diameters and rupture velocities (section 6). Finally, in sections 7 and 8, we compare the
144 data with the synthetics to determine which rupture areas are plausible and which types of LFEs
145 could match the observations.

146 **2 Premise: Mapping Inter-Station Similarity to Rupture Area**

147 In order to estimate LFE areas, we note that seismic waves generated at a range of locations
148 throughout the source region require different amounts of time to travel to the various stations. For
149 instance, in the rupture illustrated in Figure 1d, seismic waves generated by the high-slip asperity
150 marked in red arrive earliest at the NW station (left) because the asperity is in the northwestern
151 half of the rupture. But waves generated at the blue asperity, located farther SE, arrive first at the
152 SE station. The time-shifted signals give rise to apparent source time functions (ASTFs) that differ
153 among the recording stations, as seen in Figure 1a-c.

154 If we assume that Earth structure is relatively uniform within the source region, we may account
155 for the travel time variations by modeling the observed seismograms d_k in terms of station-specific
156 apparent source time functions s_k . At each station k ,

$$\hat{d}_k(\omega) = \hat{s}_k(\omega)\hat{g}_k(\omega). \quad (1)$$

157 Here g_k is an average Green's function for the source area, and \hat{d}_k , \hat{s}_k , and \hat{g}_k are the Fourier
158 coefficients of d_k , s_k , and g_k , respectively.

159 If we define $g_k(t)$ as the Green's function for a signal generated at a reference location x_0 ,
160 $\Delta t_k(x)$ as the source-station travel time for a signal generated at location x , and $\dot{\delta}(x, t)$ as the slip
161 rate as a function of location x and time t , then the ASTF can be obtained by integrating over all

162 points x within the rupture area:

$$s_k(t) = \int_{\text{rupture area}} \delta(x, t - \Delta t_k(x) + \Delta t_k(x_0)) dA. \quad (2)$$

163 The coloring in Figure 1 shows how three slip asperities shown contribute to ASTFs that differ
 164 among stations located to the northwest, southeast, and above the earthquake. Note that the asper-
 165 ities create differences at all three stations even though the earthquake ruptures radially out from
 166 the center point.

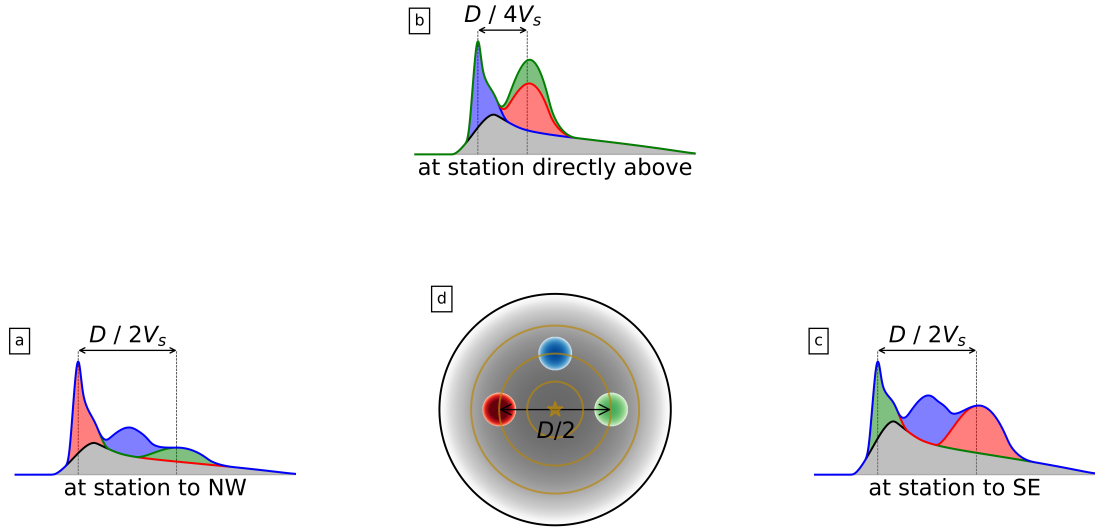


Figure 1: (a-c) ASTFs observed at 3 stations due to rupture of the slip distribution illustrated in panel (d). Rupture progresses outward from the center and moves through 3 high-slip asperities of varying magnitude, illustrated with colored circles. The asperities generate seismic waves which require different amounts of time to travel to the stations, giving rise to the various colored peaks in the ASTFs. Note that the timing of the asperity-created peaks varies among the stations by up to $D/2V_s$: half the rupture diameter divided by the shear wave speed.

167 There is, however, a limit to the ASTF differences. The spatially variable source-station travel
 168 time may shift peaks in this earthquake's source time function by only a limited amount: up to
 169 D/V_s , the rupture diameter D divided by the seismic wavespeed V_s . Thus we can see differences
 170 in the ASTFs only if we examine their short-period signal. If we examine ASTFs at periods much
 171 longer than D/V_s , the travel time shifts will be a small fraction of the period, and the ASTFs will be
 172 roughly the same at all stations. Synthetic rupture models described in section 6 show that ASTFs
 173 are similar among stations at periods longer than 0.45 to $1.4D/V_s$. Here the range of limiting
 174 periods results from the earthquakes' other rupture parameters, but we note that periods at which
 175 ASTFs are similar depend primarily on the diameter divided by seismic wave speed V_s , not on the
 176 diameter divided by the LFEs' rupture speed V_r . We will thus be able to use the ASTFs' frequency-
 177 dependent similarity to estimate LFE rupture extents without making restrictive assumptions about
 178 LFE rupture dynamics.

179 **3 Quantifying Coherence Across Events and Stations**

180 **3.1 Removing the Path Effect**

181 In order to examine ASTFs, we must first isolate them from the observed seismograms. To do
 182 so, we use an empirical Green's function approach similar to that of *Hawthorne and Ampuero*
 183 (2017) and compare each LFE's seismograms with a template event created via stacking (a variant
 184 on, e.g., *Mueller*, 1985; *Mori and Frankel*, 1990; *Velasco et al.*, 1994; *Hough*, 1997; *Prieto et al.*,
 185 2004; *Baltay et al.*, 2010; *Kwiatek et al.*, 2011; *Uchide et al.*, 2014). The individual and template
 186 LFEs' seismograms d_{jk} and d_{tk} can be approximated as convolutions of ASTFs s_{jk} or s_{tk} and
 187 Green's functions g_k , so that

$$\hat{d}_{jk}(\omega) = \hat{s}_{jk}(\omega)\hat{g}_k(\omega). \quad (3)$$

188 To isolate the ASTFs from the Green's functions, we compute the normalized cross-spectrum
 189 \hat{x}_{jk} of the individual and template recordings:

$$\hat{x}_{jk} = \frac{\hat{d}_{jk}\hat{d}_{tk}^*}{|\hat{d}_{tk}^*|^2} = \frac{\hat{s}_{jk}\hat{s}_{tk}^*|\hat{g}_k|^2}{|\hat{s}_{tk}|^2|\hat{g}_k|^2} = \frac{\hat{s}_{jk}\hat{s}_{tk}^*}{|\hat{s}_{tk}|^2}, \quad (4)$$

190 where we have omitted the frequency indexing for readability. In the second equality, we have
 191 assumed that the template LFE has the same Green's functions as the individual event, so that the
 192 path effects cancel out, and we are left with a function that depends on the relative amplitudes
 193 and phases of the individual and template ASTFs. Note that we always normalize by the template
 194 amplitude, as this will allow us to stack ASTFs from thousands of LFEs. We will use the cross-
 195 spectra \hat{x}_{jk} to examine how ASTFs' amplitudes and phases vary among LFEs j and stations k .

196 **3.2 ASTF Energy: Direct and Inter-Station Coherence**

197 As a first step, we ignore inter-station variations, and simply examine how much LFE source time
 198 functions vary from event to event. We assess the similarity between the individual and template
 199 ASTFs by computing the directly coherent power for each LFE j

$$P_d = \frac{1}{N} \sum_{k=1}^N a_{jk}^2 [\operatorname{Re}(\hat{x}_{jk})]^2 \operatorname{sgn}[\operatorname{Re}(\hat{x}_{jk})] \quad (5)$$

$$= \frac{1}{N} \sum_{k=1}^N a_{jk}^2 \left[\operatorname{Re} \frac{\hat{s}_{jk}\hat{s}_{tk}^*}{|\hat{s}_{tk}|^2} \right]^2 \operatorname{sgn}[\operatorname{Re}(\hat{s}_{jk}\hat{s}_{tk}^*)]. \quad (6)$$

200 Here the coefficients a_{jk} represent an optional weighting of the observed signals. The equality
 201 in equation (6) assumes that the individual LFE and the template have the same path effects. If
 202 the individual and template LFEs also have similar and well-aligned ASTFs \hat{s}_{jk} and \hat{s}_{tk} , the value
 203 $\hat{s}_{jk}\hat{s}_{tk}^*$ in equation (6) will be real and positive. The directly coherent power P_d is thus also positive
 204 when the individual and templates ASTFs are the same. Its amplitude is determined by the relative
 205 power of the individual and template ASTFs.

206 The relative ASTF power also determines the amplitude of the inter-station coherent power P_c .
 207 With this power calculation, we seek to ignore ASTF variations across events, and instead assess

208 the ASTFs' similarity across stations. So we compute

$$P_c = \frac{2}{N(N-1)} \sum_{k=1}^N \sum_{l=k+1}^N a_{jk} a_{jl} \operatorname{Re}(\hat{x}_{jk} \hat{x}_{jl}^*) \quad (7)$$

$$= \frac{2}{N(N-1)} \sum_{k=1}^N \sum_{l=k+1}^N a_{jk} a_{jl} \operatorname{Re} \frac{(\hat{s}_{jk} \hat{s}_{jl}^*) (\hat{s}_{tk}^* \hat{s}_{tl})}{|\hat{s}_{tk}|^2 |\hat{s}_{tl}|^2}, \quad (8)$$

209 where the second equality again assumes common path effects. As noted in section 2, the ASTFs
 210 are expected to be the same for all stations if the period being considered with these Fourier coeffi-
 211 cients is long compared with D/V_s , the intra-source seismic wave travel time. If the ASTFs are the
 212 same across stations at the period of interest, we will have $\hat{s}_{jk} = \hat{s}_{jl}$ and $\hat{s}_{tk} = \hat{s}_{tl}$, so that $\hat{s}_{jk} \hat{s}_{jl}^*$,
 213 $\hat{s}_{tk}^* \hat{s}_{tl}$, and finally P_c are all real and positive.

214 P_d and P_c thus give us estimates of the direct or inter-station coherent power of an LFE, as
 215 normalized by the template power. However, we can obtain a more interpretable normalization if
 216 we also estimate the full template-normalized LFE power, including any incoherent components:

$$P_l = \frac{1}{N} \sum_{k=1}^N a_{jk}^2 |\hat{x}_{jk}|^2 \quad (9)$$

$$= \frac{1}{N} \sum_{k=1}^N a_{jk}^2 |\hat{s}_{jk}|^2. \quad (10)$$

217 We will use the LFE power P_l to normalize P_d and P_c and compute the fraction of the power that
 218 is coherent across events and stations.

219 4 Calculating Powers of Parkfield LFEs

220 When we extract the coherent and incoherent powers of LFEs near Parkfield, we will also have to
 221 estimate and remove the noise, and we will have to average over thousands of LFEs to obtain well-
 222 resolved powers. To begin, we describe the LFE catalog and seismic data (section 4.1) and create
 223 templates for seven LFE families (section 4.2). Then we demonstrate our approach by estimating
 224 template-normalized powers for an individual LFE (section 4.3). Finally, we average the powers
 225 over the LFEs in each family (section 5).

226 4.1 Data and LFE Families

227 The LFEs considered here occurred between 2006 and 2015 at depths of 16 to 23 km near Parkfield,
 228 CA (see Figure 2). They were identified via cross-correlation by *Shelly* (2017) as part of his 15-
 229 year tremor catalog and are grouped into seven families numbered 37140, 37102, 70316, 27270,
 230 45688, 77401, and 9707, with 2500 to 8300 LFEs in each family (see also *Shelly et al.* (2009);
 231 *Shelly and Hardebeck* (2010)). LFEs in families 37140 and 37102 were examined by *Thomas*
 232 *et al.* (2016) and found to have best-fitting source durations of 0.19 and 0.22 s, respectively. We
 233 use LFE seismograms from 17 borehole seismic stations in the Berkeley HRSN (High Resolution

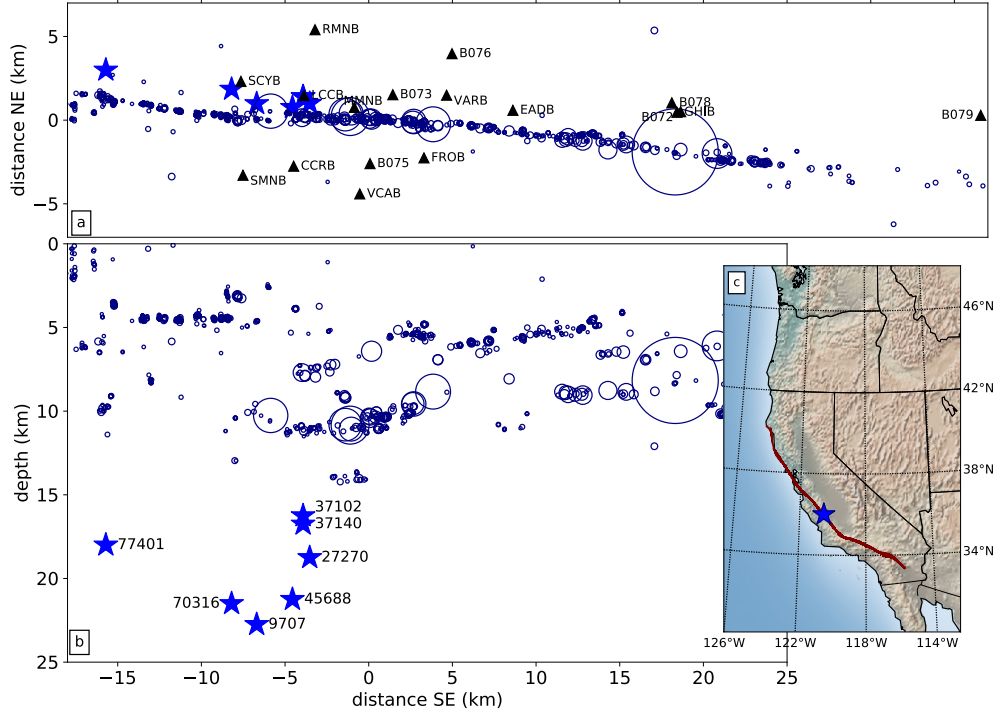


Figure 2: (a) Map view and (b) depth section of the LFE families (blue stars), local $M > 2.5$ earthquakes (circles), and the HRSN and PBO seismic stations used (triangles). Earthquake sizes are scaled to the radii expected for 3-MPa stress drops, and locations are taken from the NCEDC catalog and the relocations of *Waldhauser* (2009).

234 Seismic Network) and in the PBO (Plate Boundary Observatory) network. Since this analysis
 235 relies on high-quality recordings of small LFEs, we correct the data for some errors identified by
 236 *Shelly* (2017). We have also gone through the data from each station and channel and discarded
 237 weeks- to years-long intervals where the LFE amplitudes are much more scattered than usual, as
 238 these intervals likely have larger-than-average noise.

239 4.2 Stacked LFE Templates

240 For each LFE family, we create a low-noise template by averaging the LFE records for each chan-
 241 nel. We bandpass filter the LFE seismograms from 2 to 30 Hz, normalize them by their maximum
 242 values, and then average, weighting each record by the station-averaged cross-correlation coeffi-
 243 cient obtained by *Shelly* (2017). Then we rescale these normalized stacks so that their amplitudes
 244 match the amplitudes of individual records, as described in section S2. We iterate the stack a few
 245 times to slightly improve the signal to noise ratio, each time discarding records with very small or
 246 unusual amplitudes (for details see section S2).

247 We estimate the signal to noise ratio of the stacks using a 3-second window starting just before
 248 the S arrival. We keep only the stacks which have average amplitude spectra at least 3 times larger
 249 than the noise in the 2 to 10 Hz band. The procedure leaves us with 16 to 29 well-resolved template
 250 seismograms for each LFE family, observed on the two horizontal components of 9 to 16 stations.
 251 Some are shown in Figure 3a, as well as in Figures S1 to S7.

252 4.3 Coherent and Total Powers for One LFE

253 We will use the obtained templates to remove the Green's functions from individual LFE records,
254 so that we can probe the LFEs' ASTFs. To prepare, we realign each LFE's origin time to better
255 match the template, as poor alignment could reduce the direct coherence P_d . We bandpass filter to
256 2 to 5 Hz, cross-correlate to obtain a preferred shift at each station, and then shift the seismograms
257 of all stations by the median shift.

258 Next, we remove the path effects for the power calculations. We extract 3-second-long segments
259 of the template seismograms, starting just before the S arrival, and cross-correlate the segments
260 with the individual LFE records. The individual LFE records are truncated 0.2 seconds
261 before the S arrival to reduce contamination by the P arrival, but they are not truncated after the
262 S wave. We average the cross-correlations over the available channels at each station.

263 Cross-correlations obtained for one LFE are illustrated in Figure 3b. The cross-correlations are
264 often roughly but not entirely symmetric, suggesting that the individual and template LFEs have
265 slightly different source time functions. The asymmetry is also apparent in the non-zero phases of
266 the cross-correlations' Fourier coefficients, which are equal to the phases of the normalized cross-
267 spectra \hat{x}_{jk} (equation (4), Figure 3c). To estimate the \hat{x}_{jk} , we first extract a 6-second portion of the
268 cross-correlations, multiply by a Slepian taper concentrated at frequencies lower than 0.4 Hz, and
269 compute the Fourier transform (Thomson, 1982). Then we normalize; we divide by the Fourier
270 transform of the template seismograms' autocorrelation, computed via the same procedure.

271 We use the cross-spectra to compute the power that is directly coherent (P_d , equation (5)) and
272 coherent among stations (P_c , equation (7)) and plot them in yellow and red in Figure 3d. The total
273 power P_t in the template-normalized cross-correlation is also computed, following equation (9),
274 and is plotted in green. However, a significant fraction of this total power comes from noise, not
275 from the LFE signal. To estimate the noise contribution, we cross-correlate the template seismo-
276 grams with data from noise intervals starting 8 seconds before the S arrivals. We compute the
277 power (P_n) in those noise correlations, again following equation (9), and plot it in gray in Fig-
278 ure 3d. Finally, we subtract the noise power P_n from the total power P_t to determine the power
279 contributed by the LFE (P_l , blue in Figure 3d).

280 In all the power calculations, we use weightings a_{jk} equal to one over the standard deviation
281 of the 2 to 30-Hz filtered waveform, as computed in the four seconds ending 0.5 s before the LFE
282 S arrival. This weighting allows us to downweight records with large noise, but it does not bias our
283 results because all of the power in P_t , P_c , and P_d comes from after 0.2 s before the S arrival and
284 because almost all of the subtracted noise power P_n comes from more than 5 seconds before the S
285 arrival.

286 In an ideal scenario, we would now interpret the estimated powers, and compare the coherent
287 powers P_d and P_c with the LFE power P_l . However, for this and other individual LFEs, the powers
288 are too poorly resolved to allow direct interpretation. In Figure 3d, the ratios P_d/P_l and P_c/P_l
289 vary by tens of percent among the frequencies but show no systematic trend, and there is further
290 variation if we use different subsets of the stations. So in the next section, we will average the
291 powers over several thousand LFEs to obtain well-resolved and stable coherent power fractions.

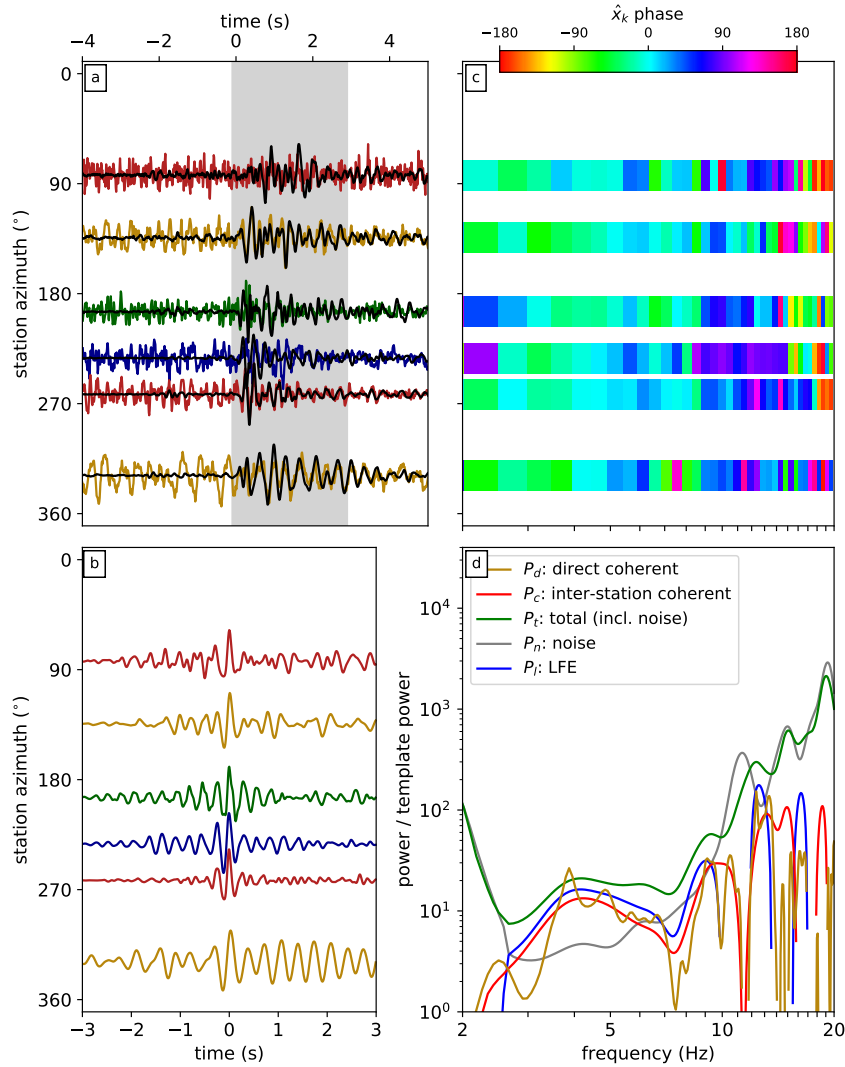


Figure 3: (a) Some of the template seismograms (black) for family 37102 along with seismograms observed for one LFE (color). Traces are organized according to the station's azimuth relative to the LFE and are scaled to their maximum value. The gray shading indicates the portion of the template that is correlated with the individual observations. (b) Cross-correlations of the observed seismograms with the template. (c) Phase of the cross-spectra: of the Fourier coefficients of the cross-correlations in panel b. (d) Yellow, red, and green curves: P_d , P_c , and P_t —the coherent and total template-normalized powers from the LFE interval. Gray: P_n —the noise power, computed in an interval without the LFE. Blue: $P_l = P_t - P_n$ —the power likely contributed by the LFE. Note that with just this one LFE, it is not practical to interpret the relative values of the coherent and total powers.

292 5 Results: Event-Averaged Coherent and Incoherent Powers

293 To estimate P_c , P_d , P_t , and P_n for a given family of LFEs, we compute the powers for individual
294 events and then average. However, some LFE records have exceptionally large noise, so we check
295 the signals' amplitudes before the calculation and discard records when the S arrival or the preceding
296 noise interval has standard deviation that differs by more than a factor of 10 from that channel's
297 median. This record selection, coupled with data availability, leaves us with 860 to 4220 LFEs per
298 family which have template-normalized powers computed from at least 5 stations.

299 Figure 4a shows the summed coherent and total powers obtained from 2000 LFEs in fam-
300 ily 37140, one of the two families with duration estimates from *Thomas et al.* (2016). The shading
301 indicates 95% uncertainty ranges on the powers, obtained by bootstrapping the LFEs included in
302 the summation. All of the template-normalized powers increase with frequency, suggesting that
303 the high-frequency template power is damped relative to a typical LFE. The stacks' high-frequency
304 signal may be averaged out by stacking if LFEs are more different at higher frequencies or if the
305 LFE timing is not accurate enough to allow coherent stacks at higher frequencies. The stack-
306 ing effectively creates a template LFE which has slightly broader and simpler ASTFs (*Royer and*
307 *Bostock*, 2014). Note that this ASTF modification may reduce the direct coherence between the
308 template and the individual LFEs P_d , but it should not affect the inter-station coherence P_c , as P_c
309 is independent of inter-event ASTF differences.

310 We compute the coherent power fractions P_d/P_l and P_c/P_l for all 7 families and plot the
311 results in Figure 4b-h. For family 37140 (panel b), the direct coherence P_d/P_l is larger than 0.8
312 at frequencies of 2 to 4 Hz, suggesting that most 0.2-second-long LFE source time functions are
313 similar when viewed at these frequencies. We should note, however, that P_d/P_l may be slightly
314 higher than its true value in this range because we allowed for an LFE origin time shift using data
315 in the 2 to 5-Hz range. P_d/P_l decreases at higher frequencies, falling below 0.6 at a frequency of
316 5 Hz. The decrease in direct coherence could imply (1) that the LFE source time functions are more
317 different at higher frequencies, (2) that the LFEs are too poorly aligned to show direct coherence at
318 high frequencies, or (3) that the stacking has modified the source time functions being compared.
319 We have tried improving the alignment by using higher-frequency signals in the alignment cross-
320 correlation, outside the 2 to 5-Hz range. We find that the high-frequency signals does result in large
321 P_d/P_l out to higher frequencies, but we choose not to use it here because some of the increase in
322 P_d/P_l could come from the alignment of high-frequency noise.

323 Family 37140's inter-station coherent power P_c/P_l is insensitive to the alignment, and it re-
324 mains coherent over a wider frequency range. P_c/P_l is above 0.8 at frequencies up to 12 or 15 Hz
325 and falls below 0.6 only at 16.5 Hz. The persistence of high P_c/P_l out to frequencies >15 Hz
326 suggests that the ASTFs vary little among stations at >0.07 -second periods. We will use synthetic
327 rupture calculations to interpret this high-frequency coherence in terms of LFE rupture area in
328 section 7.

329 The other six LFE families show similar or slightly lower coherence, as seen in Figure 4c-h
330 and in Figures S8 - S14. Family 37102, the other family with an estimated duration (*Thomas et al.*,
331 2016), displays gradually decaying P_d/P_l and P_c/P_l (Figures 4b and S9). Its P_d/P_l falls below
332 0.6 at 4 Hz, and its P_c/P_l stays above or hovers near 0.6 until 9 Hz. For the remaining families,
333 the direct coherence P_d/P_l remains above 0.6 out to 4 to 5 Hz. The inter-station coherence P_c/P_l
334 remains above 0.6 out to 8 to 13 Hz: to 8, 9, 11, 12, and 13 Hz.

335 These high-coherence frequency limits are likely lower bounds on the true high-coherence fre-

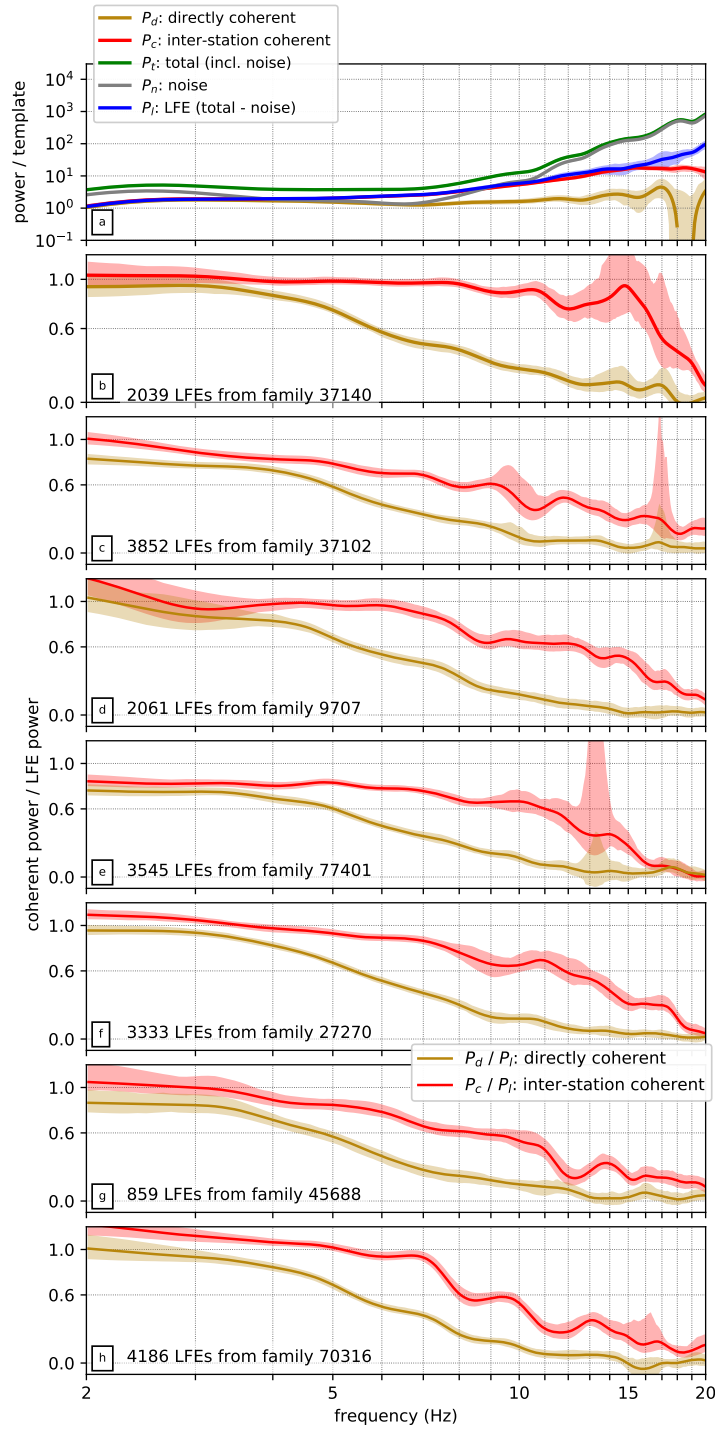


Figure 4: (a) Coherent and incoherent powers, as in Figure 3d, but averaged over 2000 LFEs from family 37140. Color indicates the power of interest. In all panels, the line indicates the value obtained with all allowable LFEs, and the shaded region delimits 95% confidence intervals obtained by bootstrapping the included events. (b-h) Ratios of the direct and inter-station coherence: P_c/P_t (yellow) and P_d/P_t (red). Each panel is computed for a different LFE family, as indicated by the text in the bottom left.

336 quencies. Our coherence estimates could be affected by several factors, including LFE clustering,
 337 data selection, LFE origin time alignment, and template accuracy. We describe the uncertainties
 338 in Appendix A1 and note that only the LFE origin time alignment is likely to give artificially high
 339 coherence, and it affects only P_d/P_l , not P_c/P_l . The remaining factors would result in our un-
 340 derestimating the true P_d/P_l and P_c/P_l . In section 7, we will therefore interpret our coherence
 341 estimates as lower limits when we consider their implications for LFE rupture areas and location
 342 distributions.

343 6 Frequencies With Coherent Power: Synthetics

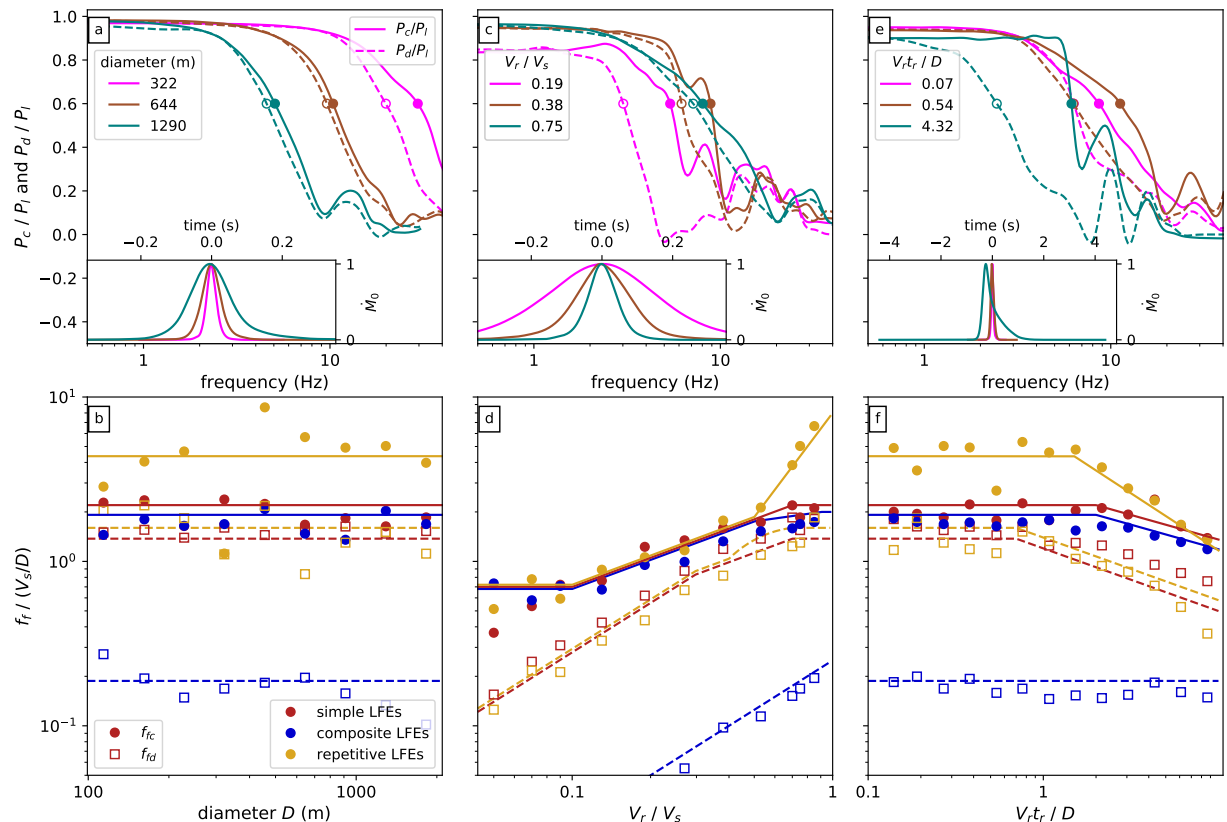


Figure 5: (a, c, e) Coherent power fractions P_c/P_l (solid lines) and P_d/P_l (dashed lines) as a function of frequency for various groups of synthetic LFEs. Circles mark the coherence falloff frequencies: when P_c/P_l or P_d/P_l falls below 0.6. Inset panels show the moment rate functions averaged over LFEs in each group. Color indicates diameter (panel a), rupture velocity (panel c), and rise time (panel e). (b, d, f) Normalized coherence falloff frequencies $f_{fc}/(V_s/D)$ (filled circles) and $f_{fd}/(V_s/D)$ (open squares) as a function of the LFE properties. Color indicates the type of LFE rupture. Solid and dashed lines indicate approximations of the numerically identified f_{fc} and f_{fd} to be used in our interpretations. In panels a, b, c, and d, $t_r = 0.27D/V_r$. In panels a, b, e, and f, $V_r = 0.75V_s$. In panels c and e, $D = 456$ m. In panels d and f, the values plotted are medians taken from synthetics with 7 different diameters.

344 To consider the coherence's implications for LFE rupture areas, we need to know how P_d/P_l
345 and P_c/P_l depend on LFE rupture properties. So we generate and analyze groups of synthetic LFEs
346 with various diameters D , rupture velocities V_r , and rise times t_r . We create synthetic ruptures for
347 three types of LFEs (section 6.1), analyze their waveforms (section 6.2), and examine the coherent
348 frequencies as a function of the LFE properties (section 6.3).

349 6.1 Synthetic LFEs Models

350 We create and analyze groups of 100 LFEs. The individual events are assigned diameters D ,
351 rupture velocities V_r , and rise times t_r that cluster around specified mean values. The diameters,
352 rupture velocities, and rise times are chosen from lognormal distributions with factor of 1.3, 1.1,
353 and 1.3 standard deviations, respectively. Moments are chosen from lognormal distributions with
354 factor of 1.5 standard deviation and assigned with no consideration of the radii.

355 In the simplest version of our LFEs, each event is assigned a random heterogeneous slip dis-
356 tribution within a roughly circular area, as detailed in section S4 and motivated by inferences of
357 fractal earthquake slip distributions (Frankel, 1991; Herrero and Bernard, 1994; Mai and Beroza,
358 2002). Rupture initiates at a random location within $0.4D$ of the center and spreads radially at rate
359 V_r . Once a location starts slipping, slip accumulates following a regularized Yoffe function with
360 duration t_r (Tinti *et al.*, 2005).

361 We also construct groups of LFEs with more repetitive rupture patterns, as it is possible that
362 LFEs within a given family recur not just on the same patch, but with similar rupture patterns within
363 that patch (e.g., Ariyoshi *et al.*, 2009; Ando *et al.*, 2010; Sweet *et al.*, 2014; Chestler and Creager,
364 2017b). In our repetitive LFEs, slip is the sum of two heterogeneous distributions: one that varies
365 randomly from event to event and one that is the same from event to event. The distributions
366 are scaled so that the repetitive component contributes twice as much moment, and slip always
367 nucleates within $0.1D$ of the LFE center points.

368 Finally, we construct groups of composite LFEs, as it is possible that individual LFEs comprise
369 a series of small ruptures of the complex fault zone at depth (Fagereng *et al.*, 2014; Hayman and
370 Lavier, 2014; Chestler and Creager, 2017b; Rubin and Bostock, 2017). Each of our relatively
371 crude composite LFE contains five simple ruptures whose rupture velocities, diameters, and slip
372 distributed are chosen from the lognormal and heterogeneous distributions described above. The
373 five sub-ruptures begin at random times within a $2.5D/V_r$ interval.

374 6.2 Computing and Analyzing LFE Waveforms

375 Having defined the location and timing of slip in the LFEs, we compute ASTFs for nearby stations.
376 We assume that the synthetic LFEs are in the location of family 37140 and calculate ASTFs for the
377 12 stations used in its analysis, as shown in Figures 2 and S1. To calculate ASTFs, we integrate
378 the slip rate over the slipping area at each time step, but shift the signals' arrival times to account
379 for the travel time from each point in the source region to the observing stations, as in equation (2).
380 To calculate seismograms, we convolve these ASTFs with fake Green's functions, which are taken
381 to be white noise tapered by an exponential with a 3-s decay constant.

382 We may now process the synthetic seismograms. As with the real data, we create templates for
383 each LFE group, normalizing the synthetic seismograms by their maximum values and stacking.
384 We iterate this stack three times. Each time, we cross-correlate the template seismograms with

385 the individual LFEs' waveforms. We identify a station-averaged time shift for each LFE, realign
386 according to those shifts, and stack.

387 Next, we use the templates to compute the cross-spectrum \hat{x}_{jk} for each synthetic LFE record
388 (equation (4)). As with the real data, we compute the cross-spectra from the tapered cross-
389 correlations, but we adjust the taper duration to ensure that it is always significantly longer than
390 the LFEs' durations. Finally, we compute the LFEs' template-normalized powers P_c , P_d , and P_l
391 (equations (5), (7), and (9)). Figure 5a, c, and e shows the coherent power fractions P_d/P_l and
392 P_c/P_l obtained for simple LFEs with various diameters, rupture velocities, and rise times.

393 6.3 Coherence Falloff Frequencies as a Function of D , V_r , and t_r

394 6.3.1 Coherence Falloff with Diameter

395 As anticipated in section 2, both P_d/P_l and P_c/P_l decrease at lower frequencies (longer periods)
396 when the LFE diameters are larger (panel a). P_d/P_l falls off earlier when diameters are larger
397 because larger diameters imply longer ruptures, which allow for complexity and inter-LFE vari-
398 ability at lower frequencies. P_c/P_l falls off earlier because larger diameters imply larger shifts
399 in the source-station travel time within the rupture area, and thus allow for inter-station ASTF
400 variability at lower frequencies. To examine the coherence falloff systematically, we identify the
401 frequencies at which P_d/P_l and P_c/P_l first fall below 0.6. These falloff frequencies f_{fd} and f_{fc} are
402 normalized by V_s/D and plotted as a function of LFE diameter D in Figure 5b. In the simple LFE
403 simulations in Figure 5b, which have $V_r/V_s = 0.75$ and $t_r = 0.27R/V_r$, f_{fd} is roughly $1.4V_s/D$
404 (open red squares and dashed red line), and f_{fc} is roughly $2.2V_s/D$ (filled red circles and solid red
405 line).

406 Note that these ratios $f_{fd}/(V_s/D)$ and $f_{fc}/(V_s/D)$ could change slightly if we assumed a
407 different distribution of stations, as different takeoff angles and azimuths could change the apparent
408 source durations and travel time shifts. Here we have chosen a station distribution consistent with
409 the stations used in analyzing the Parkfield data.

410 6.3.2 Coherence Falloff with Rupture Velocity

411 The direct coherence falloff frequency f_{fd} decreases relative to V_s/D if LFE rupture velocities
412 are reduced, as shown Figure 5c and d. Note that when we plot $f_{fd}/(V_s/D)$ and $f_{fc}/(V_s/D)$ in
413 Figure 5d and f, we take the median of estimates computed for 7 groups of LFEs, with different
414 diameters, in order to reduce the scatter. The decrease of $f_{fd}/(V_s/D)$ with decreasing rupture
415 velocities arises because lower rupture velocities allow for longer ruptures and therefore more
416 complexity and inter-event variability at lower frequencies. The LFEs' heterogeneous slip distri-
417 butions give rise to source time functions that differ among events at all frequencies shorter than
418 the rupture duration, which scales as D/V_r in simulations of simple LFEs. The direct coherence
419 falloff frequency f_{fd} thus scales inversely with the durations of these ruptures, with value around
420 $2.8V_r/D$ when $V_r < 0.4V_s$, though it decreases relative to V_r/D for rupture velocities larger than
421 $0.8V_s$ (red dashed line in Figure 5d).

422 The inter-station coherence falloff frequency f_{fc} depends more weakly on rupture velocity V_r .
423 f_{fc} increases from 0.7 to $2.2V_s/D$ as V_r increases from 0.05 to $1V_s$ (filled red circles and solid
424 red line in Figure 5d). P_c/P_l depends only weakly on V_r because P_c/P_l measures how much

425 the ASTFs vary among stations, not among events. The inter-station ASTF variability depends
426 primarily on the S-wave travel time across the source region, which scales with D/V_s , not D/V_r .
427 The V_r dependence that does exist likely results from the simpler ASTF pulses associated with
428 higher rupture velocities. As V_r approaches V_s , the ASTFs tend toward single pulses, and inter-
429 station complexity is harder to distinguish.

430 6.3.3 Coherence Falloff With Rise Time

431 Both f_{fd} and f_{fc} vary minimally in response to modest changes in the duration t_r of slip at each
432 point in the rupture, especially when the rise time t_r is less than D/V_r (Figure 5c and f). In
433 our implementation, we have assumed a spatially uniform rise time for each LFE. As a result,
434 changing the rise time is roughly equivalent to convolving all of an LFE's ASTFs by a single
435 function, and such a convolution has little effect on the inter-ASTF coherence. We do allow roughly
436 10% variability in rise time and rupture velocity among the LFEs in each group. These rise time
437 differences, coupled with the increased complexity visible in longer-duration ruptures, are likely
438 responsible for the reduced coherence falloff frequencies that become apparent once t_r exceeds 1
439 to $2D/V_r$. (red symbols and lines in Figure 5d).

440 6.3.4 LFE Durations

441 Increasing the rise time does increase LFE durations. To estimate durations for each LFE group,
442 we stack the events' source time functions using the same alignment used in the stack creation.
443 Then we identify the time interval containing the central 70% of the LFE moment. In our simple
444 LFEs, these intervals have durations that increase from between 0.29 and $0.31D/V_r$ when t_r is
445 $0.27D/V_r$ to roughly $0.28t_r$ as t_r gets longer than D/V_r . LFE durations are shorter when we
446 require that LFEs nucleate near the rupture centers. For our modeled repetitive LFEs, which we
447 assume nucleate within $0.1D$ of their center points, durations are 0.25 to $0.28D/V_r$ when t_r is
448 $0.27D/V_r$. If we instead specify nucleation locations within $0.1D$ of the rupture edge, durations
449 are 0.35 to $0.37D/V_r$. The durations of composite LFEs are determined by the number and timing
450 of subevents. The presented LFEs, containing 5 subevents, have durations between 3 and $3.3D/V_r$.

451 6.3.5 Composite LFEs

452 The composite LFEs, with their long, complex ruptures, have reduced direct coherence. The direct
453 coherence falloff frequency f_{fd} is around $0.25V_r/D$ for all simulated events (open blue squares
454 and dashed lines in Figure 5b, d, and f). On the other hand, the inter-station falloff frequencies
455 f_{fc} are similar for simple and composite LFEs (filled blue circles and solid blue line). Here again
456 P_c/P_l depends primarily on D/V_s : on how much the source-station travel time can shift peaks in
457 the source time functions.

458 6.3.6 Repetitive LFEs

459 The coherent power fractions P_d/P_l and P_c/P_l can be significantly higher for repetitive LFEs,
460 at least when the rupture velocity is larger than about $0.5V_s$. As described in section 6.1, the
461 repetitive LFEs in each group have similar slip distributions, and they all nucleate near the rupture
462 center, so they have similar ASTFs and similar waveforms. This similarity explains the increase in

463 P_d/P_l , but the increase in P_c/P_l is surprising at first glance, as P_c/P_l measures similarity across
464 stations, not across events. However, the cross-spectra calculation that goes into P_c (equation (4))
465 is designed to remove complexity associated with the path effects, and it identifies as “path effect”
466 any component of the source-path convolution (equation (3)) that is common to all events. If
467 the ASTFs are the same for all events, the P_c calculation cannot distinguish inter-station ASTF
468 variations from station-dependent Green’s functions, ASTF variations are thus attributed to path
469 effects, and P_c/P_l is high when LFEs are highly repetitive. The falloff frequencies f_{fc} can increase
470 by a factor of 6 when $V_r > 0.8V_s$.

471 We note, however, that this factor of 6 increase in f_{fc} is just one plausible value. Here we have
472 assumed that two-thirds of the LFE moment came from a repetitive component of the rupture, but
473 higher or lower coherence could be achieved by assuming that more or less of the moment came
474 from the repetitive component. We also note that the high coherence arises only when the rupture
475 nucleation location is consistent from event to event. The falloff frequencies f_{fc} remain low if only
476 75% of the repetitive LFEs nucleate at the SE rupture edge and the other 25% nucleate on the NW
477 edge (Figure S22).

478 7 Interpretation of LFE Coherence

479 We may now use our synthetic results to interpret the coherence obtained for the Parkfield LFE
480 families, which show direct coherence $P_d/P_l > 0.5$ out to 4 to 5 Hz and inter-station coherence
481 $P_c/P_l > 0.5$ out to 8 to 16.5 Hz.

482 7.1 LFE Location Distribution

483 First, we note that the observed high-frequency coherence implies that LFEs within each family are
484 strongly clustered in space. If LFEs were distributed over a wide range of locations, travel times
485 from the LFE centroids to the recording stations would vary widely from event to event. But in our
486 analysis, we allow only the origin time to be realigned from event to event. Any inter-station time
487 shifts produced by varying LFE locations should show up in our results as a decrease in coherence.

488 To determine the maximum location variation allowed by the observations, we recompute co-
489 herence values after artificially shifting the LFE locations by various amounts. We pick location
490 shifts for each LFE in family 37140, drawing from bivariate normal distributions with 100-m to
491 1-km standard deviations along strike and depth. We use the IASP91 velocity model and TauP
492 to compute the arrival time change for the stations observing each LFE (*Kennett and Engdahl,*
493 1991; *Crotwell et al.*, 1999). We subtract the median arrival time change from these values, shift
494 the seismograms by the station-dependent remainders, and compute the coherent power fractions.
495 The family-averaged results are shown in Figures 6 and S15-S17. We find that the inter-station
496 coherent fraction P_c/P_l obtained at 11 Hz is reduced by 40% even for location shifts with just
497 250-m standard deviation (Figure 6). The > 0.6 11-Hz coherence values obtained for the median
498 family thus imply that LFEs in each family are strongly clustered, with standard deviation in their
499 locations typically smaller than 250 m.

500 Note that the distribution of LFE locations within a family, when coupled with noise, is one
501 way to explain all of the incoherence observed at higher frequencies in the data. It is possible that

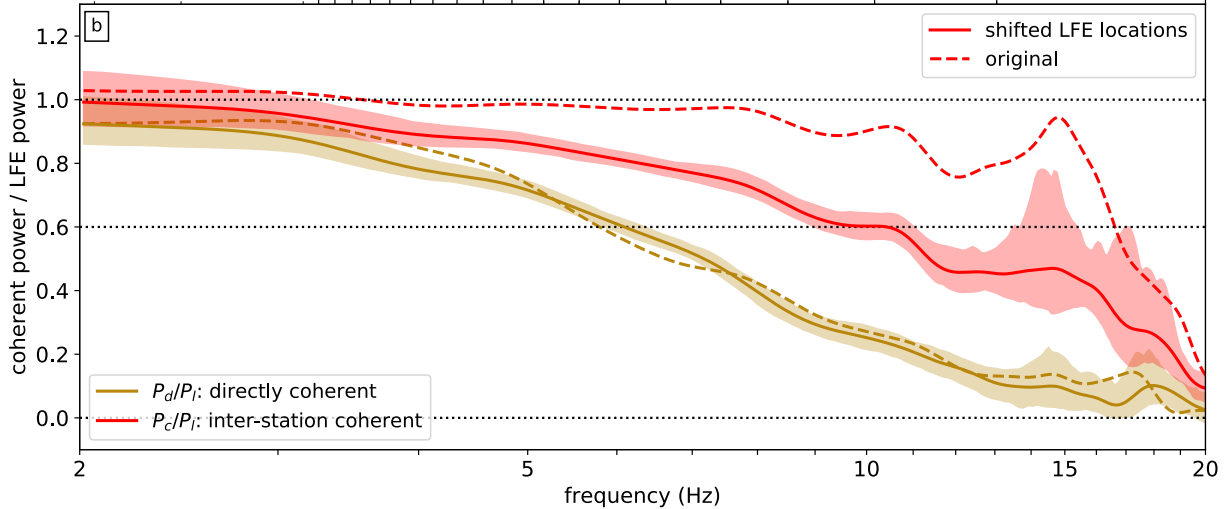


Figure 6: Solid lines and shading: coherent power fractions for family 37140, as in Figure 4b, but computed after shifting the LFE locations by random amounts with 250-m standard deviations along strike and along depth. Dashed lines: original P_d/P_l and P_c/P_l , without location shifts, reproduced from Figure 4b.

502 the individual LFEs appear to be point sources—that each LFE ruptures a tiny patch within the
 503 sub-1-km asperity (*Chestler and Creager, 2017a*).

504 7.2 Matching f_{fc} , f_{fd} , and Duration With Simple Ruptures: Results

505 However, it is also possible that the finite rupture areas of individual LFEs contribute to the de-
 506 crease in coherence at high frequencies. To determine the maximum rupture areas and rupture
 507 velocities allowed by the data, we compare the observed coherence falloff frequencies and dura-
 508 tions with those obtained from synthetics of simple, non-repetitive ruptures.

509 First, we note that the inter-station coherence P_c/P_l remains higher than 0.6 out to 8 to 16.5 Hz
 510 for the various families. The median P_c/P_l falloff frequency f_{fc} is 11 Hz, and families 37102
 511 and 37140, which we will discuss in more detail, have f_{fc} of 9 and 16.5 Hz, respectively. In the
 512 synthetics, f_{fc} is 0.7 to $2.2V_s/D$ for rupture velocities V_r between 0.05 and $1V_s$ (red solid line
 513 in Figure 5d). If the shear wave velocity V_s is around 4 km/s in the LFE area (*Lin et al., 2010*),
 514 family 37102’s 9-Hz f_{fc} implies an average diameter smaller than 300 to 1000 m, with smaller
 515 allowable diameters for slower rupture velocities. In Figure 7a, this range of allowable diameters
 516 is marked with blue diagonal hatching. The thicker blue line presents alternative upper bound on
 517 the diameter, ranging from 180 to 550 m. It is appropriate for a 16-Hz f_{fc} : the bootstrap-estimated
 518 lower bound on f_{fc} obtained for family 37140.

519 The yellow diagonal hatching in Figure 7a illustrates a further, albeit weaker, constraint on the
 520 LFEs’ diameters and rupture velocities: those obtained from the direct coherence P_d/P_l . P_d/P_l
 521 is higher than 0.6 out to 4 to 5 Hz for all seven LFE families, though it could be biased high or
 522 low by uncertainties in the LFE origin time alignment (see Appendix A1). In the synthetics, the
 523 P_d/P_l falloff frequency f_{fd} scales roughly with 1 over duration. It ranges from 1.4 to $2.8V_r/D$,

524 or from 0.15 to $1.4V_s/D$ (blue dashed line in Figure 5d). Coupling the synthetics with a 5-Hz f_{fd}
525 constrains the LFE diameters to be less than 1100 m.

526 More important constraints on the LFE properties come from the LFE durations estimated
527 by Thomas *et al.* (2016). Thomas *et al.* (2016) compared LFE stacks with nearby earthquakes' waveforms
528 and obtained best-fitting durations of 0.19 and 0.22s for LFEs in families 37140 and 37102, respectively. To get a sense of the uncertainty, we note that their best fits come from
529 averaging over comparisons with 12 or 17 different local earthquakes, but they also present the
530 durations obtained by the individual earthquake comparisons. Only one earthquake comparison
531 gives a family 37140 duration smaller than 0.15 or larger than 0.22, and only one comparison
532 gives a family 37102 duration smaller than 0.15 or larger than 0.3, so we use these values as
533 uncertainty bounds. To compare the durations to our synthetics, we note that 70% of the moment
534 in the stacked synthetic LFEs accumulates within 0.29 to $0.31V_r/D$. Thomas *et al.* (2016) modeled
535 the LFE waveforms with a Hann-like source time function, which accumulates 70% of its moment
536 within 40% of length, so the 70% durations for families 37140 and 37102 are 0.060 to 0.087 and
537 0.060 to 0.12 s, respectively. We multiply these 70% durations by 1.4 to $2.8V_r$ to estimate LFE
538 diameters and plot the results with red vertical hatching in Figure 7a. The lower and upper thick
539 red lines mark the diameters expected for the best-fitting durations for families 37140 and 37102,
540 respectively.

541 The diameters implied by the observed durations match those implied by family 37102's > 9 Hz f_{fc} for a wide range of rupture velocities. The two sets of constraints overlap at least partially
542 for all plotted V_r/V_s , and the inter-station coherence constraint matches the median duration when
543 $V_r < V_s$. According to these results, LFEs in family 37102 could be slow ruptures, with 200-m
544 diameters and $V_r = 0.2V_s$. Or they could be relatively "normal" earthquakes, with 800-m
545 diameters and $V_r = 0.8V_s$. Note that changing the assumed shear wave velocity V_s would change
546 the estimated diameters in Figure 7, but not the V_r/V_s intersection ranges, as all of the plotted
547 diameter constraints scale with $1/V_s$.

548 Given the uncertainties in the data, the constraints on LFEs in family 37140 could also be
549 matched with a range of rupture speeds. This family's $f_{fc} \gtrsim 16$ Hz constraint (below the solid blue
550 line) starts to intersect the duration constraints when $V_r < 0.7V_s$. However, we should note that the
551 plotted 16-Hz constraint is already the 95% lower bound on f_{fc} , obtained from bootstrapping. The
552 best-fitting f_{fc} is 16.5 Hz. Further, the $f_{fc} \gtrsim 16$ Hz constraint intersects the best-fitting duration
553 only when $V_r < 0.4V_s$. Family 37140's data are thus best matched when $V_r < 0.4V_s$.

556 7.3 Matching f_{fc} , f_{fd} , and Duration With Simple Ruptures: Uncertainties

557 To further assess whether earthquake-like rupture velocities V_r of 0.7 to $0.9V_s$ are plausible, not
558 just possible, for family 37140, we consider additional sources of uncertainty in the duration- and
559 coherence-derived diameters. The diameters implied by the durations would decrease slightly if all
560 ruptures began at the asperity edge. Groups of synthetic ruptures starting within $0.1D$ of the LFE
561 edge have durations of 0.35 to $0.37D/V_r$, rather than the 0.29 to $0.31D/V_r$ values estimated for
562 events starting within $0.4D$ of the center. However, synthetic ruptures starting from the edge also
563 give f_{fc} values about 20% smaller than those starting closer to the center (Figure S19). Changing
564 both constraints leaves the range of allowable rupture velocities almost unchanged.

565 Other minor modifications to the rupture parameters appear to affect the f_{fc} constraints min-
566 imally. For instance, we observe little change in f_{fc} if we add a smooth tapered component to

567 the heterogeneous slip distributions (Figure S21) or if we limit the range of diameters within each
568 group to a factor of 1.1 standard deviation (Figure S23). However, we have not explored the
569 entire range of rupture parameters. Perhaps we would obtain higher coherence if we made the
570 slip distribution and temporal evolution smoother or slightly more repetitive, more similar to the
571 repeater-like LFEs discussed in sections 6.1 and 7.4.

572 Another scenario that seems unlikely but possible is that the 16.5-Hz f_{fc} obtained for family
573 37140 reflects random variability. This f_{fc} is significantly larger than the median f_{fc} for the seven
574 families, which is just 11-Hz, and the synthetics in Figure 5b do show tens of percent variability in
575 f_{fc} among LFE groups, simply as a result of random variations in the slip distributions. However,
576 those synthetics use only 100 LFEs. Using several thousand should reduce the uncertainty. Further,
577 bootstrapping events within each synthetic group gives a reasonable estimate of the variability
578 among the groups. Bootstrapping the data in family 37140 gives 95% probability that $f_{fc} > 16$ Hz.

579 The other uncertainties in the data, along with potential variation in LFE location, would imply
580 that the estimated 16.5-Hz f_{fc} is a lower bound on the true value, as discussed in section 5 and
581 appendix A1. Given these uncertainties, we cannot exclude the possibility that these LFEs are
582 simple ruptures with “typical” earthquake rupture speeds around $0.7V_s$. But we consider it more
583 likely that the rupture velocities are lower than $0.7V_s$. The data are best matched by simple LFEs
584 when rupture velocities are less than $0.4V_s$.

585 7.4 Matching the Data With Modified LFE Ruptures

586 It is also possible to match the data if we modify the LFE dynamics significantly: if LFEs are
587 composite ruptures, ruptures with long rise times, or repetitive ruptures, as described in section 6.1.
588 Figure 7b-d illustrate the constraints obtained for some plausible rupture parameters.

589 Figure 7b illustrates the constraints on diameters and rupture velocity if LFEs are composed
590 of 5 sub-ruptures distributed over an interval with duration $2.5D/V_r$. Here the inter-station coher-
591 ence constraints (blue) are essentially unchanged, but the direct coherence and duration constraints
592 imply smaller diameters.

593 Figure 7c illustrates the constraints if LFEs have rise times equal to $5D/V_r$. In these LFEs,
594 rupture would progress to the asperity edge, and then the whole patch would continue slipping
595 together.

596 Finally, Figure 7d illustrates the constraints on D and V_r/V_s if LFEs are repetitive ruptures,
597 which persistently nucleate in the same region, and which have two-thirds of their moment is
598 associated with a slip distribution that is consistent from event to event. With these repetitive
599 ruptures, the 16-Hz f_{fc} of family 37140 can be matched even if the rupture diameters are larger.

600 A wide range of parameters could also match the data if LFE durations are actually reflections
601 of local attenuation, not the LFE source dynamics (Gomberg *et al.*, 2012; Bostock *et al.*, 2017). In
602 this case, the diameters estimated from the durations (red lines) are upper bounds, and the data can
603 be matched by any combination of rupture velocity and diameter that plots below those bounds
604 and within the f_{fc} (blue) and f_{fd} (red) constraints.

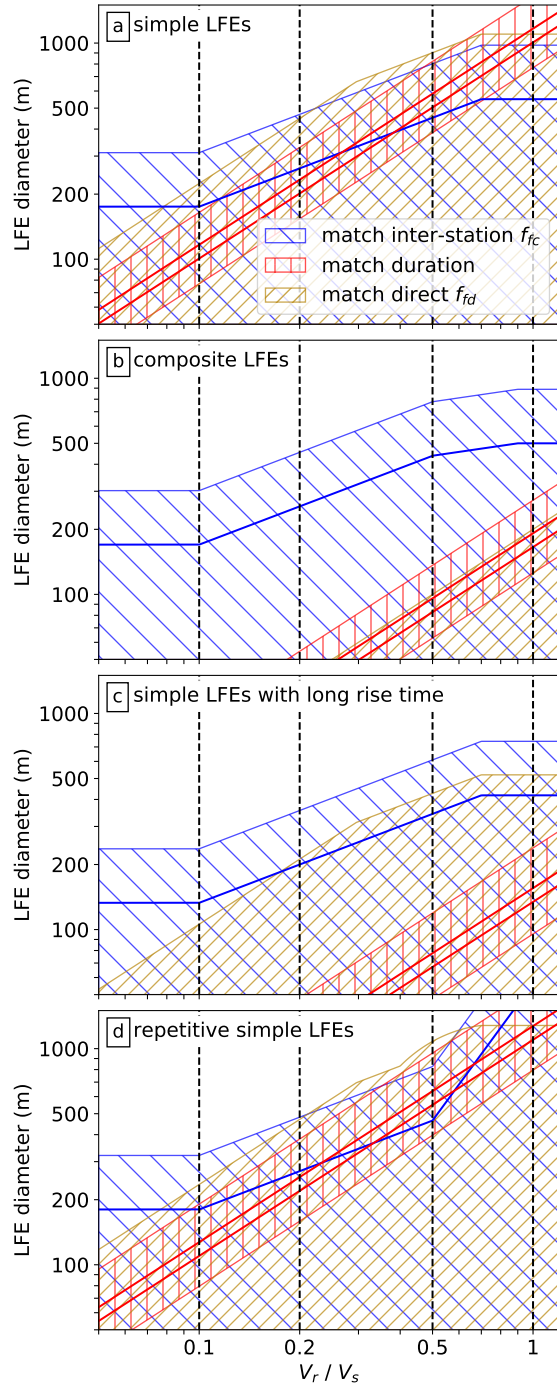


Figure 7: Hatched regions mark diameters (y-axis) and rupture velocities (x-axis) that match each of the 3 observations: f_{fc} (blue diagonal lines), f_{fd} (yellow diagonal lines), and the durations of Thomas et al. (2016) (red vertical lines). The four panels are for four approaches to constructing the LFEs, as indicated by the text in the upper left.

605 **8 Discussion**

606 **8.1 Implications for Tremor Asperities**

607 Regardless of the individual LFE rupture dynamics, our observations of high-frequency coherence
608 suggest that LFEs are clustered in patches less than 1 km across. As noted in the introduction, such
609 clustering has also been inferred by careful analysis of LFE families in Cascadia (*Sweet et al.*, 2014;
610 *Chestler and Creager*, 2017a) and may be suggested by highly periodic LFE ruptures in Parkfield
611 (*Shelly*, 2010b). The clustering may suggest a role for material heterogeneity in controlling the
612 occurrence of tremor. It is consistent with proposals that tremor's LFEs rupture a collection of
613 unstable asperities embedded in a larger, more stable region (*Ando et al.*, 2010; *Nakata et al.*,
614 2011; *Ando et al.*, 2012; *Ariyoshi et al.*, 2012; *Veedu and Barbot*, 2016; *Luo and Ampuero*, 2017).
615 Larger asperities may also exist, as patches of tremor are observed on scales of a few to tens of
616 km. The larger tremor patches could represent groups of tremor asperities or regions more prone
617 to distributed rapid slip (*Shelly*, 2010b; *Ghosh et al.*, 2012; *Armbruster et al.*, 2014; *Yabe and
618 Ide*, 2014; *Savard and Bostock*, 2015; *Annoura et al.*, 2016; *Kano et al.*, 2018). Alternatively,
619 the large and small tremor patches could represent persistent slip patterns that have arisen on a
620 simple, homogeneous fault. Such patterns are sometimes seen in models that lack heterogeneity in
621 material properties (*Horowitz and Ruina*, 1989; *Langer et al.*, 1996; *Shaw and Rice*, 2000), though
622 it remains to be assessed whether these models can produce clusters of tremor that persist over
623 many slow slip cycles, as we observe in Parkfield.

624 The family-based clustering implied by our coherence estimates and by others' LFE relocations
625 (*Sweet et al.*, 2014; *Chestler and Creager*, 2017a) suggests that cross-correlation based LFE
626 families are more an observational convenience (*Shelly et al.*, 2007; *Brown et al.*, 2008; *Bostock
627 et al.*, 2012; *Frank et al.*, 2013; *Kato*, 2017; *Shelly*, 2017). The analyzed families show sub-km LFE
628 clustering even though some are separated from neighboring families by a few to 5 km. The LFEs'
629 tendency to occur on these asperities lends further confidence to studies that have interpreted LFE
630 repeat rates as indicators of the slip rate in a creeping area surrounding the more unstable LFE
631 patches (*Rubin and Armbruster*, 2013; *Royer et al.*, 2015; *Lengliné et al.*, 2017; *Thomas et al.*,
632 2018).

633 **8.2 Implications for Tremor Physics**

634 Given our observations and synthetics of LFE coherence as a function of rupture diameter, there
635 are still several ways to explain the long, 0.2-s durations of Parkfield LFEs. First, it is possible that
636 families 37102 and 37140's LFEs are normal earthquakes with near-shear-wave rupture speeds.
637 A $0.7V_s$ rupture speed is at the edge of the constraints for family 37140, but such rapid ruptures
638 could match the data better if the LFEs are somewhat repetitive, with nucleation locations and
639 slip distributions that persist from event to event. And a wide range of high rupture speeds could
640 match the data if the 0.2-s durations we use are overestimates of the true durations, despite *Thomas
641 et al.* (2016)'s careful empirical Green's function analysis. The durations could be overestimated
642 if a highly attenuating region is localized around the LFE patches, so that attenuation removes the
643 high-frequency components of the LFE seismograms but has little effect on the seismograms of
644 the reference earthquakes, which are located a few km away.

645 If LFEs do have durations of 0.2 s and rupture speeds up to $0.7V_s$, they could have diameters

646 up to 800 m. Uniform stress drop M_w 1 to 2 earthquakes with 800-m diameters would have stress
647 drops of 0.3 to 9 kPa and average slips of 0.002 to 0.06 mm (*Eshelby*, 1957; *Shearer*, 2009). These
648 moment and slip estimates are imprecise, and difficult to estimate because LFE locations are offset
649 from local earthquakes, but we note that if the larger slip estimates are representative, almost all of
650 the slip on the LFE patch could be seismic. Even 800-m-wide LFEs could accommodate most of
651 the long-term slip on the LFE patch, which *Thomas et al.* (2016) estimated to be around 0.05 mm
652 per event.

653 But while LFEs from both families can be matched by rupture velocities up to $0.7V_s$, the data
654 from family 37140 are better matched by LFEs with slower rupture speeds ($< 0.4V_s$), long rise
655 times, or a composite of subevents. Any of these scenarios would have interesting implications
656 for the physics of LFE ruptures. For instance, rupture speeds around $0.4V_s$, which can match the
657 data for both families, would suggest that the LFEs' radiation efficiency is around 0.5: that about
658 half of the energy in LFEs is released via seismic wave generation, with the rest expended as
659 fracture energy (e.g., *Kostrov*, 1966; *Eshelby*, 1969; *Fossum and Freund*, 1975; *Venkataraman and*
660 *Kanamori*, 2004; *Kanamori and Rivera*, 2006). Such low but significant radiation efficiency could
661 mean that LFEs are exceptionally weak but otherwise normal earthquakes. LFEs may be driven
662 by unstable frictional sliding, and their slip rates may be limited by the dissipation of energy via
663 seismic waves. Although $0.4V_s$ is lower than typical earthquake rupture speeds (*McGuire*, 2004;
664 *Seekins and Boatwright*, 2010; *Folesky et al.*, 2016; *Ye et al.*, 2016; *Melgar and Hayes*, 2017;
665 *Chouimet et al.*, 2018), such speeds are sometimes observed in earthquakes, especially in shallow
666 tsunami earthquakes (e.g., *Ide et al.*, 1993; *Ihmlé et al.*, 1998; *Venkataraman and Kanamori*, 2004;
667 *Bilek and Engdahl*, 2007; *Polet and Kanamori*, 2009; *Cesca et al.*, 2011).

668 It is thus possible that LFEs are simply earthquakes driven by a frictional weakening process
669 that is for some reason smaller in magnitude than the processes driving normal earthquakes. LFEs
670 might nucleate "earlier" than most earthquakes, at times when there is only a modest stress drop
671 available to drive rupture. Or LFEs could nucleate on small unstable patches but then move quickly
672 into regions that resist high slip speeds, perhaps because they are velocity-strengthening or allow
673 for large off-fault deformation. Such acceleration-resisting regions have been suggested to limit the
674 rupture velocities of tsunami earthquakes (e.g., *Bilek and Lay*, 2002; *Faulkner et al.*, 2011a; *Ma*,
675 2012). Off-fault deformation seems an appealing process to invoke for tremor because complex
676 brittle and ductile deformation is observed at relevant depths (*Fusseis et al.*, 2006; *Handy et al.*,
677 2007; *Collettini et al.*, 2011; *Fagereng et al.*, 2014; *Hayman and Lavier*, 2014; *Angiboust et al.*,
678 2015; *Behr et al.*, 2018; *Webber et al.*, 2018). It is even possible that each LFE is a collection
679 of small brittle failures, rupturing small faults or veins (*Fagereng et al.*, 2014; *Ujiie et al.*, 2018).
680 However, it remains unclear how or if that distributed ductile deformation would limit the rupture
681 speeds of LFEs. Off-fault ductile deformation can also accumulate in large earthquakes, with
682 near-shear-wave rupture speeds (*DeDontney et al.*, 2011; *Dunham et al.*, 2011; *Roten et al.*, 2017).

683 Another possibility is that LFEs do rupture at near-shear-wave speeds, but that the shear wave
684 speed is significantly reduced in the LFE area because of lithological variations, fault zone damage,
685 or high pore pressures (*Audet et al.*, 2009; *Song et al.*, 2009; *Kato et al.*, 2010; *Fagereng and Di-*
686 *ener*, 2011; *Stefano et al.*, 2011; *Huang et al.*, 2014). Fault damage zones are frequently observed
687 at a range of depths (*Shipton and Cowie*, 2001; *Rowe et al.*, 2009; *Faulkner et al.*, 2011b; *Rempe*
688 *et al.*, 2013; *Leclère et al.*, 2015), and they sometimes show 30 to 50% reductions in wavespeed, at
689 least in shallow regions (*Ben-Zion et al.*, 2003; *Cochran et al.*, 2009; *Lewis and Ben-Zion*, 2010;
690 *Yang et al.*, 2014; *Li et al.*, 2016). It is difficult to fully assess a low-wavespeed region's implica-

tions for our observations. The inter-station coherence we observe depends on the seismic waves' source-station travel times, and those times depend on which source-station paths are traveled. But in the simplest case, where LFE signals begin by traveling horizontally away from the fault, so that they move outside the fault zone before continuing to the surface, the travel time variation we probe with inter-station coherence would depend primarily on the higher wavespeed outside the fault zone. The higher wavespeeds could allow for the high-frequency inter-station coherence we observe even though the lower wave speed inside the fault zone limits the rupture velocity and produces long-duration events.

On the other hand, it is possible that LFE rupture velocities are not limited by seismic wave radiation at all, but by a different fault zone rheology. We note that the results from family 37140 are best fit by simple LFE ruptures with $V_r < 0.4V_s$, and because of noise in the data, all of our coherence-constrained diameters and rupture speeds are upper bounds on the true values. So LFE rupture speeds could be much smaller: $0.2V_s$, for example. Such slowly rupturing LFEs would release more than 80% of their energy via fracture energy, making it unlikely that the energy dissipated via seismic wave radiation could limit the slip speeds. The low rupture velocities inferred for family 37140 could be telling us that LFE rupture dynamics are controlled by a different deformation mechanism than normal earthquakes—perhaps by the same speed-limiting rheology that controls slow slip events (e.g., *Ide et al.*, 2007; *Shibazaki and Iio*, 2003; *Shibazaki and Shimamoto*, 2007; *Ide et al.*, 2008; *Aguiar et al.*, 2009; *Liu et al.*, 2010; *Segall et al.*, 2010; *Gao et al.*, 2012; *Hawthorne and Rubin*, 2013; *Ide and Yabe*, 2014; *Hawthorne and Bartlow*, 2018).

9 Conclusions

We have analyzed inter-station and inter-event coherence between LFEs in seven families near Parkfield, CA. Our synthetic analysis shows that we can use inter-station ASTF variations to estimate LFE or earthquake rupture areas. Our observations of LFE coherence imply that LFEs in each family are strongly clustered, with standard deviation in their locations smaller than 250 m. Comparing the observed coherence with that of synthetic LFE ruptures implies that the LFE diameters are smaller than 500 to 1100 m, depending on the family. Coupling the coherence constraints with the LFE durations estimated by *Thomas et al.* (2016) suggests that we could match the data for LFEs in family 37102 with a wide range of rupture models, including earthquake-like ruptures with rupture velocities V_r of 0.7 to 0.9 times the shear wave speed V_s . For family 37140, $V_r = 0.7V_s$ can match the data, but only on the edge of the constraints, and the data are better matched with $V_r < 0.4V_s$. Such low rupture speeds may indicate that LFEs are governed by a slow slip rheology, not by standard unstable frictional sliding, but we note that data from both families of LFEs could also be matched if LFEs are repetitive fast ruptures, composite ruptures, or ruptures with long rise times. Our synthetics illustrate how the coherence and durations might differ among these rupture types, and thus how we might probe the physics of LFEs with future observations.

Acknowledgments

We also used seismic waveform data from the Berkeley Parkfield High Resolution Seismic Network (HRSN), provided via the Northern California Earthquake Data Center and the Berkeley

730 Seismological Laboratory (doi: 10.7932/NCECD), as well as seismic waveform data from the
731 Plate Boundary Observatory (PBO) borehole seismic network, operated by UNAVCO and funded
732 by NSF grant EAR-0732947. The PBO data was obtained via IRIS. The fault traces shown in
733 Figure 2 were obtained from the USGS and California Geological Survey fault and fold database,
734 accessed from <http://earthquake.usgs.gov/hazards/qfaults> in 2016.

735 A1 Decoherence from Noise

736 Our coherence frequencies should probably be interpreted as lower bounds, as several sources of
737 noise could reduce the observed P_d/P_l and P_c/P_l from their true values. First, decreased P_d/P_l
738 and P_c/P_l could arise if a significant portion of the “noise” comes from LFEs that are nearby but
739 not in the family of interest. LFEs are clustered in space and time (e.g., *Shelly*, 2010a; *Bostock*
740 *et al.*, 2015) so the noise from other LFEs may be higher during the LFE window than during the
741 noise window before it. We estimate the noise power P_n in a window that starts just 8 s before the
742 LFE S arrival to minimize the potential difference, but we cannot account for sub-8 s clustering.
743 Note that in principle our noise window could include some of the P arrival. However, we find
744 the P arrival is too late and too small to significantly affect the P_n estimates. Truncating the noise
745 waveforms before the P arrivals and reprocessing changes our results negligibly.

746 Decreased P_d/P_l and P_c/P_l could also result from noise in the template LFEs. The template
747 signals start to become poorly resolved at frequencies higher than 15 Hz, so it is difficult to calcu-
748 late robust powers at those frequencies.

749 Finally, decreased or increased P_d/P_l could result from uncertainty in the LFE origin time. To
750 accurately calculate direct coherence at high frequencies, we need well aligned waveforms, so we
751 re-compute LFE origin times using 0.01-s precision. The realignment affects P_c/P_l negligibly but
752 increases the frequencies with $P_d/P_l > 0.5$ by several Hz relative to results without recomputed
753 origin time. One might worry that the increase in coherence comes from aligning the template
754 with coherent noise rather than with LFE signal. However, we require at least 5 stations for the
755 power estimates for each LFE, and we allow only one origin time shift per LFE. Assuming noise
756 is random among stations, realigning with noise should increase P_d/P_l by less than 0.2.

757 The LFE detection approach of *Shelly* (2017) could also result in slightly increased coherence
758 if noise contributes a part of the identified coherent signals. Finally, slightly increased coherence
759 could result from our exclusion of signals with especially high noise. Note that the detected-
760 facilitated increases in coherence are most likely to occur at low frequencies, around a few Hz, as
761 these frequencies contribute most of the seismogram power involved in LFE selection and align-
762 ment.

763 There are no other obvious sources of artificially high coherence. Applying our processing to
764 noise intervals rather than LFEs gives P_c/P_l and P_d/P_l of 0.01 or less.

765 References

766 Aguiar, A. C., T. I. Melbourne, and C. W. Scrivner, Moment release rate of Cascadia tremor con-
767 strained by GPS, *J. Geophys. Res.*, 114, B00A05, doi:10.1029/2008JB005909, 2009.

- 768 Ando, R., R. Nakata, and T. Hori, A slip pulse model with fault heterogeneity for low-
769 frequency earthquakes and tremor along plate interfaces, *Geophys. Res. Lett.*, 37, L10310, doi:
770 10.1029/2010GL043056, 2010.
- 771 Ando, R., N. Takeda, and T. Yamashita, Propagation dynamics of seismic and aseismic slip gov-
772 erned by fault heterogeneity and Newtonian rheology, *J. Geophys. Res.*, 117(B11), B11308,
773 doi:10.1029/2012JB009532, 2012.
- 774 Angiboust, S., J. Kirsch, O. Oncken, J. Glodny, P. Monié, and E. Rybacki, Probing the transition
775 between seismically coupled and decoupled segments along an ancient subduction interface,
776 *Geochem., Geophys., Geosyst.*, 16(6), 1905–1922, doi:10.1002/2015GC005776, 2015.
- 777 Annoura, S., K. Obara, and T. Maeda, Total energy of deep low-frequency tremor in the
778 Nankai subduction zone, southwest Japan, *Geophys. Res. Lett.*, 43(6), 2562–2567, doi:
779 10.1002/2016GL067780, 2016.
- 780 Ariyoshi, K., T. Hori, J.-P. Ampuero, Y. Kaneda, T. Matsuzawa, R. Hino, and A. Hasegawa,
781 Influence of interaction between small asperities on various types of slow earthquakes in
782 a 3-D simulation for a subduction plate boundary, *Gondwana Res.*, 16(3-4), 534–544, doi:
783 10.1016/j.gr.2009.03.006, 2009.
- 784 Ariyoshi, K., T. Matsuzawa, J.-P. Ampuero, R. Nakata, T. Hori, Y. Kaneda, R. Hino, and
785 A. Hasegawa, Migration process of very low-frequency events based on a chain-reaction model
786 and its application to the detection of preseismic slip for megathrust earthquakes, *Earth Planets
787 Space*, 64(8), 693–702, doi:10.5047/eps.2010.09.003, 2012.
- 788 Armbruster, J. G., W.-Y. Kim, and A. M. Rubin, Accurate tremor locations from coherent S and P
789 waves, *J. Geophys. Res.*, 119(6), 5000–5013, doi:10.1002/2014JB011133, 2014.
- 790 Audet, P., and A. J. Schaeffer, Fluid pressure and shear zone development over the locked to slow
791 slip region in Cascadia, *Science Advances*, 4(3), eaar2982, doi:10.1126/sciadv.aar2982, 2018.
- 792 Audet, P., M. G. Bostock, N. I. Christensen, and S. M. Peacock, Seismic evidence for over-
793 pressured subducted oceanic crust and megathrust fault sealing, *Nature*, 457, 76–78, doi:
794 10.1038/nature07650, 2009.
- 795 Baltay, A., G. Prieto, and G. C. Beroza, Radiated seismic energy from coda measurements
796 and no scaling in apparent stress with seismic moment, *J. Geophys. Res.*, 115, B08314, doi:
797 201010.1029/2009JB006736, 2010.
- 798 Behr, W. M., A. J. Kotowski, and K. T. Ashley, Dehydration-induced rheological heterogene-
799 ity and the deep tremor source in warm subduction zones, *Geology*, 46(5), 475–478, doi:
800 10.1130/G40105.1, 2018.
- 801 Bell, R., R. Sutherland, D. H. N. Barker, S. Henrys, S. Bannister, L. Wallace, and J. Beavan,
802 Seismic reflection character of the Hikurangi subduction interface, New Zealand, in the region
803 of repeated Gisborne slow slip events, *Geophys. J. Intern.*, 180(1), 34–48, doi:10.1111/j.1365-
804 246X.2009.04401.x, 2010.

- 805 Ben-Zion, Y., Z. Peng, D. Okaya, L. Seeber, J. G. Armbruster, N. Ozer, A. J. Michael, S. Baris, and
806 M. Aktar, A shallow fault-zone structure illuminated by trapped waves in the Karadere–Duzce
807 branch of the North Anatolian Fault, western Turkey, *Geophys. J. Intern.*, 152(3), 699–717,
808 doi:10.1046/j.1365-246X.2003.01870.x, 2003.
- 809 Bilek, S. L., and E. R. Engdahl, Rupture characterization and aftershock relocations for the 1994
810 and 2006 tsunami earthquakes in the Java subduction zone, *Geophys. Res. Lett.*, 34(20), doi:
811 10.1029/2007GL031357, 2007.
- 812 Bilek, S. L., and T. Lay, Tsunami earthquakes possibly widespread manifestations of frictional
813 conditional stability, *Geophys. Res. Lett.*, 29(14), 1–4, doi:10.1029/2002GL015215, 2002.
- 814 Bostock, M. G., A. A. Royer, E. H. Hearn, and S. M. Peacock, Low frequency earthquakes
815 below southern Vancouver Island, *Geochem., Geophys., Geosyst.*, 13(11), Q11007, doi:
816 10.1029/2012GC004391, 2012.
- 817 Bostock, M. G., A. M. Thomas, G. Savard, L. Chuang, and A. M. Rubin, Magnitudes and moment-
818 duration scaling of low-frequency earthquakes beneath southern Vancouver Island, *J. Geophys.
819 Res.*, 120(9), 6329–6350, doi:10.1002/2015JB012195, 2015.
- 820 Bostock, M. G., A. M. Thomas, A. M. Rubin, and N. I. Christensen, On corner frequen-
821 cies, attenuation, and low-frequency earthquakes, *J. Geophys. Res.*, 122(1), 543–557, doi:
822 10.1002/2016JB013405, 2017.
- 823 Brown, J. R., G. C. Beroza, and D. R. Shelly, An autocorrelation method to detect low frequency
824 earthquakes within tremor, *Geophys. Res. Lett.*, 35(16), L16305, doi:10.1029/2008GL034560,
825 2008.
- 826 Brown, J. R., G. C. Beroza, S. Ide, K. Ohta, D. R. Shelly, S. Y. Schwartz, W. Rabbel, M. Thorwart,
827 and H. Kao, Deep low-frequency earthquakes in tremor localize to the plate interface in multiple
828 subduction zones, *Geophys. Res. Lett.*, 36, L19306, doi:10.1029/2009GL040027, 2009.
- 829 Cesca, S., T. Dahm, C. Juretzek, and D. Kühn, Rupture process of the 2001 May 7 Mw
830 4.3 Ekofisk induced earthquake, *Geophys. J. Intern.*, 187(1), 407–413, doi:10.1111/j.1365-
831 246X.2011.05151.x, 2011.
- 832 Chamberlain, C. J., D. R. Shelly, J. Townend, and T. A. Stern, Low-frequency earthquakes reveal
833 punctuated slow slip on the deep extent of the Alpine Fault, New Zealand, *Geochem., Geophys.,
834 Geosyst.*, 15(7), 2984–2999, doi:10.1002/2014GC005436, 2014.
- 835 Chestler, S. R., and K. C. Creager, Evidence for a scale-limited low-frequency earthquake source
836 process, *J. Geophys. Res.*, 122(4), 3099–3114, doi:10.1002/2016JB013717, 2017a.
- 837 Chestler, S. R., and K. C. Creager, A model for low-frequency earthquake slip, *Geochem., Geo-
838 phys., Geosyst.*, 18(12), 4690–4708, doi:10.1002/2017GC007253, 2017b.
- 839 Chouimet, A., M. Vallée, M. Causse, and F. Courboulex, Global catalog of earthquake rupture
840 velocities shows anticorrelation between stress drop and rupture velocity, *Tectonophysics*, 733,
841 148–158, doi:10.1016/j.tecto.2017.11.005, 2018.

- 842 Cochran, E. S., Y.-G. Li, P. M. Shearer, S. Barbot, Y. Fialko, and J. E. Vidale, Seismic and
843 geodetic evidence for extensive, long-lived fault damage zones, *Geology*, 37(4), 315–318, doi:
844 10.1130/G25306A.1, 2009.
- 845 Collettini, C., A. Niemeijer, C. Viti, S. A. Smith, and C. Marone, Fault structure, frictional prop-
846 erties and mixed-mode fault slip behavior, *Earth Planet. Sci. Lett.*, 311(3–4), 316–327, doi:
847 10.1016/j.epsl.2011.09.020, 2011.
- 848 Crotwell, H. P., T. J. Owens, and J. Ritsema, The TauP toolkit: flexible seismic travel-time and
849 ray-path utilities, *Seis. Res. Lett.*, 70(2), 154–160, doi:10.1785/gssrl.70.2.154, 1999.
- 850 DeDontney, N., E. L. Templeton-Barrett, J. R. Rice, and R. Dmowska, Influence of plastic de-
851 formation on bimaterial fault rupture directivity, *J. Geophys. Res.*, 116(B10), B10312, doi:
852 10.1029/2011JB008417, 2011.
- 853 Dunham, E. M., D. Belanger, L. Cong, and J. E. Kozdon, Earthquake ruptures with strongly rate-
854 weakening friction and off-fault plasticity, Part 1: Planar faults, *Bull. Seis. Soc. Amer.*, 101(5),
855 2296–2307, doi:10.1785/0120100075, 2011.
- 856 Eshelby, J. D., The determination of the elastic field of an ellipsoidal inclusion, and related prob-
857 lems, *Proc. Roy. Soc. London. Series A. Mathematical and Physical Sciences*, 241(1226), 376–
858 396, doi:10.1098/rspa.1957.0133, 1957.
- 859 Eshelby, J. D., The elastic field of a crack extending non-uniformly under general anti-plane
860 loading, *Journal of the Mechanics and Physics of Solids*, 17(3), 177–199, doi:10.1016/0022-
861 5096(69)90032-5, 1969.
- 862 Fagereng, Å., and J. F. A. Diener, San Andreas Fault tremor and retrograde metamorphism, *Geo-
863 phys. Res. Lett.*, 38(23), L23303, doi:10.1029/2011GL049550, 2011.
- 864 Fagereng, Å., G. W. B. Hillary, and J. F. A. Diener, Brittle-viscous deformation, slow slip, and
865 tremor, *Geophys. Res. Lett.*, 41(12), 4159–4167, doi:10.1002/2014GL060433, 2014.
- 866 Faulkner, D. R., T. M. Mitchell, J. Behnsen, T. Hirose, and T. Shimamoto, Stuck in the mud? Earth-
867 quake nucleation and propagation through accretionary forearcs, *Geophys. Res. Lett.*, 38(18),
868 L18303, doi:10.1029/2011GL048552, 2011a.
- 869 Faulkner, D. R., T. M. Mitchell, E. Jensen, and J. Cembrano, Scaling of fault damage zones with
870 displacement and the implications for fault growth processes, *J. Geophys. Res.*, 116, B05403,
871 doi:10.1029/2010JB007788, 2011b.
- 872 Fletcher, J. B., and A. McGarr, Moments, magnitudes, and radiated energies of non-volcanic
873 tremor near Cholame, CA, from ground motion spectra at UPSAR, *Geophys. Res. Lett.*, 38(16),
874 L16314, doi:10.1029/2011GL048636, 2011.
- 875 Folesky, J., J. Kummerow, S. A. Shapiro, M. Häring, and H. Asanuma, Rupture directivity of fluid-
876 induced microseismic events: Observations from an enhanced geothermal system, *J. Geophys.
877 Res.*, 121(11), 8034–8047, doi:10.1002/2016JB013078, 2016.

- 878 Fossum, A. F., and L. B. Freund, Nonuniformly moving shear crack model of a shallow focus
879 earthquake mechanism, *J. Geophys. Res.*, 80(23), 3347, doi:10.1029/JB080i023p03343, 1975.
- 880 Frank, W. B., N. M. Shapiro, V. Kostoglodov, A. L. Husker, M. Campillo, J. S. Payero, and G. A.
881 Prieto, Low-frequency earthquakes in the Mexican Sweet Spot, *Geophys. Res. Lett.*, 40(11),
882 2661–2666, doi:10.1002/grl.50561, 2013.
- 883 Frankel, A., High-frequency spectral falloff of earthquakes, fractal dimension of complex rup-
884 ture, b value, and the scaling of strength on faults, *J. Geophys. Res.*, 96, 6291–6302, doi:
885 10.1029/91JB00237, 1991.
- 886 Fry, B., K. Chao, S. Bannister, Z. Peng, and L. Wallace, Deep tremor in New Zealand trig-
887 gered by the 2010 Mw8.8 Chile earthquake, *Geophys. Res. Lett.*, 38(15), L15306, doi:
888 10.1029/2011GL048319, 2011.
- 889 Fusseis, F., M. R. Handy, and C. Schrank, Networking of shear zones at the brittle-to-viscous
890 transition (Cap de Creus, NE Spain), *Journal of Structural Geology*, 28(7), 1228–1243, doi:
891 10.1016/j.jsg.2006.03.022, 2006.
- 892 Gao, H., D. A. Schmidt, and R. J. Weldon, Scaling relationships of source parameters for slow slip
893 events, *Bull. Seis. Soc. Amer.*, 102(1), 352–360, doi:10.1785/0120110096, 2012.
- 894 Ghosh, A., J. E. Vidale, and K. C. Creager, Tremor asperities in the transition zone control evo-
895 lution of slow earthquakes, *J. Geophys. Res.*, 117(B10), B10301, doi:10.1029/2012JB009249,
896 2012.
- 897 Gomberg, J., K. Creager, J. Sweet, J. Vidale, A. Ghosh, and A. Hotovec, Earthquake spectra and
898 near-source attenuation in the Cascadia subduction zone, *J. Geophys. Res.*, 117(B5), B05312,
899 doi:10.1029/2011JB009055, 2012.
- 900 Got, J.-L., and J. Fréchet, Origins of amplitude variations in seismic doublets: Source or attenua-
901 tion process?, *Geophys. J. Intern.*, 114(2), 325–340, doi:10.1111/j.1365-246X.1993.tb03921.x,
902 1993.
- 903 Handy, M. R., G. Hirth, and R. Burgmann, Continental Fault Structure and Rheology from the
904 Frictional-to-Viscous Transition Downwards, in *Tectonic Faults: Agents of Change on a Dy-*
905 *namic Earth (Dahlem Workshop 95, Berlin, January 2005)*, edited by M. R. Handy, G. Hirth,
906 and N. Hovius, pp. 139–182, MIT Press, Cambridge, MA, 2007.
- 907 Hawthorne, J. C., and J.-P. Ampuero, A phase coherence approach to identifying co-located earth-
908 quakes and tremor, *Geophys. J. Intern.*, 209(2), 623–642, doi:10.1093/gji/ggx012, 2017.
- 909 Hawthorne, J. C., and N. M. Bartlow, Observing and modeling the spectrum of a slow slip event,
910 *J. Geophys. Res.*, 123(5), 4243–4265, doi:10.1029/2017JB015124, 2018.
- 911 Hawthorne, J. C., and A. M. Rubin, Laterally propagating slow slip events in a rate and state
912 friction model with a velocity-weakening to velocity-strengthening transition, *J. Geophys. Res.*,
913 118(7), 3785–3808, doi:10.1002/jgrb.50261, 2013.

- 914 Hayman, N. W., and L. L. Lavier, The geologic record of deep episodic tremor and slip, *Geology*,
915 42(3), 195–198, doi:10.1130/G34990.1, 2014.
- 916 Herrero, A., and P. Bernard, A kinematic self-similar rupture process for earthquakes, *Bull. Seis.
917 Soc. Amer.*, 84(4), 1216–1228, 1994.
- 918 Horowitz, F. G., and A. Ruina, Slip patterns in a spatially homogeneous fault model, *J. Geophys.
919 Res.*, 94(B8), 10,279–10,298, 1989.
- 920 Hough, S. E., Empirical Green's function analysis: Taking the next step, *J. Geophys. Res.*, 102,
921 5369–5384, doi:10.1029/96JB03488, 1997.
- 922 Huang, Y., J.-P. Ampuero, and D. V. Helmberger, Earthquake ruptures modulated by waves in
923 damaged fault zones, *J. Geophys. Res.*, 119(4), 3133–3154, doi:10.1002/2013JB010724, 2014.
- 924 Ide, S., and S. Yabe, Universality of slow earthquakes in the very low frequency band, *Geophys.
925 Res. Lett.*, 41(8), 2786–2793, doi:10.1002/2014GL059712, 2014.
- 926 Ide, S., F. Imamura, Y. Yoshida, and K. Abe, Source characteristics of the Nicaraguan
927 Tsunami Earthquake of September 2, 1992, *Geophys. Res. Lett.*, 20(9), 863–866, doi:
928 10.1029/93GL00683, 1993.
- 929 Ide, S., G. C. Beroza, D. R. Shelly, and T. Uchide, A scaling law for slow earthquakes, *Nature*,
930 447(7140), 76–79, doi:10.1038/nature05780, 2007.
- 931 Ide, S., K. Imanishi, Y. Yoshida, G. C. Beroza, and D. R. Shelly, Bridging the gap between seis-
932 mically and geodetically detected slow earthquakes, *Geophys. Res. Lett.*, 35(10), L10305, doi:
933 10.1029/2008GL034014, 2008.
- 934 Ihmlé, P. F., J.-M. Gomez, P. Heinrich, and S. Guibourg, The 1996 Peru tsunamigenic earthquake:
935 Broadband source process, *Geophys. Res. Lett.*, 25(14), 2691–2694, doi:10.1029/98GL01987,
936 1998.
- 937 Kanamori, H., and E. E. Brodsky, The physics of earthquakes, *Reports on Progress in Physics*,
938 67(8), 1429–1496, doi:10.1088/0034-4885/67/8/R03, 2004.
- 939 Kanamori, H., and L. Rivera, Energy partitioning during an earthquake, *Washington DC American
940 Geophysical Union Geophysical Monograph Series*, 170, 3–13, doi:10.1029/170GM03, 2006.
- 941 Kane, D. L., P. M. Shearer, B. P. Goertz-Allmann, and F. L. Vernon, Rupture directivity of small
942 earthquakes at Parkfield, *J. Geophys. Res.*, 118(1), 212–221, doi:10.1029/2012JB009675, 2013.
- 943 Kano, M., A. Kato, R. Ando, and K. Obara, Strength of tremor patches along deep transition zone
944 of a megathrust, *Scientific Reports*, 8(1), 3655, doi:10.1038/s41598-018-22048-8, 2018.
- 945 Kato, A., Illuminating deep tremors along the Nankai subduction zone, Japan, by matched filter
946 technique, *JpGU-AGU Joint Meeting*, pp. SSS04–02, 2017.

- 947 Kato, A., T. Iidaka, R. Ikuta, Y. Yoshida, K. Katsumata, T. Iwasaki, S. Sakai, C. Thurber,
 948 N. Tsumura, K. Yamaoka, T. Watanabe, T. Kunitomo, F. Yamazaki, M. Okubo, S. Suzuki, and
 949 N. Hirata, Variations of fluid pressure within the subducting oceanic crust and slow earthquakes,
 950 *Geophys. Res. Lett.*, 37, L14310, doi:10.1029/2010GL043723, 2010.
- 951 Kennett, B. L. N., and E. R. Engdahl, Traveltimes for global earthquake location and phase identifi-
 952 cation, *Geophys. J. Intern.*, 105(2), 429–465, doi:10.1111/j.1365-246X.1991.tb06724.x, 1991.
- 953 Kitajima, H., and D. M. Saffer, Elevated pore pressure and anomalously low stress in regions
 954 of low frequency earthquakes along the Nankai Trough subduction megathrust, *Geophys. Res.
 955 Lett.*, 39(23), L23301, doi:10.1029/2012GL053793, 2012.
- 956 Kostrov, B. V., Unsteady propagation of longitudinal shear cracks, *Journal of Applied Mathematics
 957 and Mechanics*, 30(6), 1241–1248, doi:10.1016/0021-8928(66)90087-6, 1966.
- 958 Kwiatek, G., K. Plenkers, G. Dresen, and J. R. Group, Source parameters of picoseismicity
 959 recorded at Mponeng deep gold mine, South Africa: implications for scaling relations, *Bull.
 960 Seis. Soc. Amer.*, 101(6), 2592–2608, doi:10.1785/0120110094, 2011.
- 961 Langer, J. S., J. M. Carlson, C. R. Myers, and B. E. Shaw, Slip complexity in dynamic models
 962 of earthquake faults, *Proceedings of the National Academy of Sciences*, 93(9), 3825–3829, doi:
 963 10.1073/pnas.93.9.3825, 1996.
- 964 Leclère, H., F. Cappa, D. Faulkner, O. Fabbri, P. Armitage, and O. Blake, Development and main-
 965 tenance of fluid overpressures in crustal fault zones by elastic compaction and implications for
 966 earthquake swarms, *J. Geophys. Res.*, 120(6), 4450–4473, doi:10.1002/2014JB011759, 2015.
- 967 Lengliné, O., and J.-L. Got, Rupture directivity of microearthquake sequences near Parkfield, Cal-
 968 ifornia, *Geophys. Res. Lett.*, 38, L08310, doi:10.1029/2011GL047303, 2011.
- 969 Lengliné, O., W. B. Frank, D. Marsan, and J. P. Ampuero, Imbricated slip rate processes during
 970 slow slip transients imaged by low-frequency earthquakes, *Earth Planet. Sci. Lett.*, 476, 122–
 971 131, doi:10.1016/j.epsl.2017.07.032, 2017.
- 972 Lewis, M. A., and Y. Ben-Zion, Diversity of fault zone damage and trapping structures in the Park-
 973 field section of the San Andreas Fault from comprehensive analysis of near fault seismograms,
 974 *Geophys. J. Intern.*, 183(3), 1579–1595, doi:10.1111/j.1365-246X.2010.04816.x, 2010.
- 975 Li, Y.-G., R. D. Catchings, and M. R. Goldman, Subsurface fault damage zone of the 2014 Mw
 976 6.0 South Napa, California, earthquake viewed from fault-zone trapped waves, *Bull. Seis. Soc.
 977 Amer.*, 106(6), 2747–2763, doi:10.1785/0120160039, 2016.
- 978 Lin, G., C. H. Thurber, H. Zhang, E. Hauksson, P. M. Shearer, F. Waldhauser, T. M. Brocher, and
 979 J. Hardebeck, A California statewide three-dimensional seismic velocity model from both ab-
 980 solute and differential times, *Bull. Seis. Soc. Amer.*, 100(1), 225–240, doi:10.1785/0120090028,
 981 2010.

- 982 Liu, L., M. Gurnis, M. Seton, J. Saleeby, R. D. Muller, and J. M. Jackson, The role of oceanic
983 plateau subduction in the Laramide orogeny, *Nat. Geosci.*, 3(5), 353–357, doi:10.1038/ngeo829,
984 2010.
- 985 Liu, Y. J., and J. R. Rice, Aseismic slip transients emerge spontaneously in three-dimensional
986 rate and state modeling of subduction earthquake sequences, *J. Geophys. Res.*, 110, B08307,
987 doi:10.1029/2004JB003424, 2005.
- 988 Liu, Y. J., and J. R. Rice, Spontaneous and triggered aseismic deformation transients in a subduc-
989 tion fault model, *J. Geophys. Res.*, 112(B9), B09404, doi:10.1029/2007JB004930, 2007.
- 990 Luo, Y., and J.-P. Ampuero, Tremor migration patterns and the collective behavior of deep asperi-
991 ties mediated by creep, *EarthArXiv*, doi:10.17605/OSF.IO/MBCAV, 2017.
- 992 Ma, S., A self-consistent mechanism for slow dynamic deformation and large tsunami genera-
993 tion for earthquakes in the shallow subduction zone, *Geophys. Res. Lett.*, 39(11), L11310, doi:
994 10.1029/2012GL051854, 2012.
- 995 Madariaga, R., Seismic source theory, in *Treatise on Geophysics*, vol. 4: Earthquake Seismology,
996 edited by H. Kanamori and G. Schubert, p. 6054, Elsevier, Amsterdam, 2007.
- 997 Maeda, T., and K. Obara, Spatiotemporal distribution of seismic energy radiation from
998 low-frequency tremor in western Shikoku, Japan, *J. Geophys. Res.*, 114, B00A09, doi:
999 10.1029/2008JB006043, 2009.
- 1000 Mai, P. M., and G. C. Beroza, A spatial random field model to characterize complexity in earth-
1001 quake slip, *J. Geophys. Res.*, 107(B11), 2308, doi:10.1029/2001JB000588, 2002.
- 1002 McGuire, J. J., Estimating finite source properties of small earthquake ruptures, *Bull. Seis. Soc.
1003 Amer.*, 94(2), 377–393, doi:10.1785/0120030091, 2004.
- 1004 Melgar, D., and G. P. Hayes, Systematic observations of the slip pulse properties of large earth-
1005 quake ruptures, *Geophys. Res. Lett.*, 44(19), 9691–9698, doi:10.1002/2017GL074916, 2017.
- 1006 Mori, J., and A. Frankel, Source parameters for small events associated with the 1986 North Palm
1007 Springs, California, earthquake determined using empirical Green functions, *Bull. Seis. Soc.
1008 Amer.*, 80(2), 278–295, 1990.
- 1009 Mueller, C. S., Source pulse enhancement by deconvolution of an empirical Green's function,
1010 *Geophys. Res. Lett.*, 12(1), 33–36, doi:10.1029/GL012i001p00033, 1985.
- 1011 Nakata, R., R. Ando, T. Hori, and S. Ide, Generation mechanism of slow earthquakes: Numerical
1012 analysis based on a dynamic model with brittle-ductile mixed fault heterogeneity, *J. Geophys.
1013 Res.*, 116(B8), B08308, doi:10.1029/2010JB008188, 2011.
- 1014 Nowack, R. L., and M. G. Bostock, Scattered waves from low-frequency earthquakes and
1015 plate boundary structure in northern Cascadia, *Geophys. Res. Lett.*, 40(16), 4238–4243, doi:
1016 10.1002/grl.50826, 2013.

- 1017 Obara, K., Nonvolcanic deep tremor associated with subduction in southwest Japan, *Science*,
1018 296(5573), 1679–1681, doi:10.1126/science.1070378, 2002.
- 1019 Payero, J. S., V. Kostoglodov, N. Shapiro, T. Mikumo, A. Iglesias, X. Perez-Campos, and R. W.
1020 Clayton, Nonvolcanic tremor observed in the Mexican subduction zone, *Geophys. Res. Lett.*, 35,
1021 L07305, doi:10.1029/2007GL032877, 2008.
- 1022 Perfettini, H., and J. P. Ampuero, Dynamics of a velocity strengthening fault region: Im-
1023 plications for slow earthquakes and postseismic slip, *J. Geophys. Res.*, 113, B09411, doi:
1024 10.1029/2007JB005398, 2008.
- 1025 Peterson, C. L., and D. H. Christensen, Possible relationship between nonvolcanic tremor and
1026 the 1998–2001 slow slip event, south central Alaska, *J. Geophys. Res.*, 114, B06302, doi:
1027 10.1029/2008JB006096, 2009.
- 1028 Polet, J., and H. Kanamori, Tsunami earthquakes, in *Encyclopedia of complexity and systems
1029 science*, pp. 9577–9592, Springer, New York, 2009.
- 1030 Poulet, T., E. Veveakis, K. Regenauer-Lieb, and D. A. Yuen, Thermo-poro-mechanics of chemi-
1031 cally active creeping faults: 3. The role of serpentinite in episodic tremor and slip sequences, and
1032 transition to chaos, *J. Geophys. Res.*, 119(6), 4606–4625, doi:10.1002/2014JB011004, 00001,
1033 2014.
- 1034 Prieto, G. A., P. M. Shearer, F. L. Vernon, and D. Kilb, Earthquake source scaling and self-
1035 similarity estimation from stacking P and S spectra, *J. Geophys. Res.*, 109(B8), B08310, doi:
1036 10.1029/2004JB003084, 2004.
- 1037 Rempe, M., T. Mitchell, J. Renner, S. Nippes, Y. Ben-Zion, and T. Rockwell, Damage and seis-
1038 mic velocity structure of pulverized rocks near the San Andreas Fault, *J. Geophys. Res.*, 118(6),
1039 2813–2831, doi:10.1002/jgrb.50184, 2013.
- 1040 Rice, J. R., The mechanics of earthquake rupture, in *Physics of the Earth's Interior (Proc. Intl.
1041 School of Physics "E. Fermi" Course 78)*, edited by A. M. Dziewonski and E. Boschi, pp. 555–
1042 650, Italian Physical Society / North Holland Publishing Co., 1980.
- 1043 Rogers, G., and H. Dragert, Episodic tremor and slip on the Cascadia subduction zone: the chatter
1044 of silent slip, *Science*, 300(5627), 1942–1943, doi:10.1126/science.1084783, 2003.
- 1045 Roten, D., K. B. Olsen, and S. M. Day, Off-fault deformations and shallow slip deficit from dy-
1046 namic rupture simulations with fault zone plasticity, *Geophys. Res. Lett.*, 44(15), 7733–7742,
1047 doi:10.1002/2017GL074323, 2017.
- 1048 Rowe, C. D., F. Meneghini, and J. C. Moore, Fluid-rich damage zone of an ancient out-of-sequence
1049 thrust, Kodiak Islands, Alaska, *Tectonics*, 28, 1–20, doi:10.1029/2007TC002126, 2009.
- 1050 Royer, A. A., and M. G. Bostock, A comparative study of low frequency earthquake templates
1051 in northern Cascadia, *Earth Planet. Sci. Lett.*, 402, 247–256, doi:10.1016/j.epsl.2013.08.040,
1052 2014.

- 1053 Royer, A. A., A. M. Thomas, and M. G. Bostock, Tidal modulation and triggering of
1054 low-frequency earthquakes in northern Cascadia, *J. Geophys. Res.*, 120(1), 384–405, doi:
1055 10.1002/2014JB011430, 2015.
- 1056 Rubin, A. M., Episodic slow slip events and rate-and-state friction, *J. Geophys. Res.*, 113, B11414,
1057 doi:10.1029/2008JB005642, 2008.
- 1058 Rubin, A. M., Properties of Creep Fronts on Rate-and-State Faults, *Eos Trans. AGU, Fall Meeting
1059 Suppl.*, 21, T21F–08, 2009.
- 1060 Rubin, A. M., and J. G. Armbruster, Imaging slow slip fronts in Cascadia with high pre-
1061 cision cross-station tremor locations, *Geochem., Geophys., Geosyst.*, pp. 5371–5392, doi:
1062 10.1002/2013GC005031, 2013.
- 1063 Rubin, A. M., and M. G. Bostock, What is This Thing Called Tremor?, *Eos Trans. AGU, Fall
1064 Meeting Suppl.*, 52, 2017.
- 1065 Rubinstein, J. L., D. R. Shelly, and W. L. Ellsworth, Non-volcanic tremor: a window into the roots
1066 of fault zones, in *New Frontiers in Integrated Solid Earth Sciences*, edited by J. Negendank and
1067 S. Cloetingh, pp. 287–314, Springer, Dordrecht, 2009.
- 1068 Saffer, D. M., and L. M. Wallace, The frictional, hydrologic, metamorphic and thermal habitat of
1069 shallow slow earthquakes, *Nat. Geosci.*, 8(8), 594–600, doi:10.1038/ngeo2490, 2015.
- 1070 Savard, G., and M. G. Bostock, Detection and location of low-frequency earthquakes using cross-
1071 station correlation, *Bull. Seis. Soc. Amer.*, 105(4), 2128–2142, doi:10.1785/0120140301, 2015.
- 1072 Seekins, L. C., and J. Boatwright, Rupture directivity of moderate earthquakes in northern Califor-
1073 nia, *Bull. Seis. Soc. Amer.*, 100(3), 1107–1119, doi:10.1785/0120090161, 2010.
- 1074 Segall, P., A. M. Rubin, A. M. Bradley, and J. R. Rice, Dilatant strengthening as a mechanism for
1075 slow slip events, *J. Geophys. Res.*, 115, B12305, doi:10.1029/2010JB007449, 2010.
- 1076 Seno, T., and T. Yamasaki, Low-frequency tremors, intraslab and interplate earthquakes in South-
1077 west Japan-from a viewpoint of slab dehydration, *Geophys. Res. Lett.*, 30(22), 1–4, doi:
1078 10.1029/2003GL018349, 2003.
- 1079 Shaw, B. E., and J. R. Rice, Existence of continuum complexity in the elastodynamics of repeated
1080 fault ruptures, *J. Geophys. Res.*, 105(B10), 23,791–23,810, doi:10.1029/2000JB900203, 2000.
- 1081 Shearer, P., *Introduction to Seismology*, 2 ed., Cambridge University Press, Cambridge, UK, 2009.
- 1082 Shelly, D. R., Migrating tremors illuminate complex deformation beneath the seismogenic San
1083 Andreas fault, *Nature*, 463(7281), 648–652, doi:10.1038/nature08755, 2010a.
- 1084 Shelly, D. R., Periodic, chaotic, and doubled earthquake recurrence intervals on the deep San
1085 Andreas Fault, *Science*, 328(5984), 1385–1388, doi:10.1126/science.1189741, 2010b.

- 1086 Shelly, D. R., A 15 year catalog of more than 1 million low-frequency earthquakes: Tracking
1087 tremor and slip along the deep San Andreas Fault, *J. Geophys. Res.*, 122(5), 3739–3753, doi:
1088 10.1002/2017JB014047, 2017.
- 1089 Shelly, D. R., and J. L. Hardebeck, Precise tremor source locations and amplitude variations
1090 along the lower-crustal central San Andreas Fault, *Geophys. Res. Lett.*, 37, L14301, doi:
1091 10.1029/2010GL043672, 2010.
- 1092 Shelly, D. R., G. C. Beroza, S. Ide, and S. Nakamura, Low-frequency earthquakes in Shikoku,
1093 Japan, and their relationship to episodic tremor and slip, *Nature*, 442(7099), 188–191, doi:
1094 10.1038/nature04931, 2006.
- 1095 Shelly, D. R., G. C. Beroza, and S. Ide, Non-volcanic tremor and low-frequency earthquake
1096 swarms, *Nature*, 446(7133), 305–307, doi:10.1038/nature05666, 2007.
- 1097 Shelly, D. R., W. L. Ellsworth, T. Ryberg, C. Haberland, G. S. Fuis, J. Murphy, R. M. Nadeau,
1098 and R. Bürgmann, Precise location of San Andreas Fault tremors near Cholame, California
1099 using seismometer clusters: Slip on the deep extension of the fault?, *Geophys. Res. Lett.*, 36(1),
1100 L01303, doi:10.1029/2008GL036367, 2009.
- 1101 Shibazaki, B., and Y. Iio, On the physical mechanism of silent slip events along the deeper part of
1102 the seismogenic zone, *Geophys. Res. Lett.*, 30(9), 1–4, doi:10.1029/2003GL017047, 2003.
- 1103 Shibazaki, B., and T. Shimamoto, Modelling of short-interval silent slip events in deeper sub-
1104 duction interfaces considering the frictional properties at the unstable-stable transition regime,
1105 *Geophys. J. Intern.*, 171(1), 191–205, doi:10.1111/j.1365-246X.2007.03434.x, 2007.
- 1106 Shipton, Z. K., and P. A. Cowie, Damage zone and slip-surface evolution over μm to km scales
1107 in high-porosity Navajo sandstone, Utah, *Journal of Structural Geology*, 23(12), 1825–1844,
1108 doi:10.1016/S0191-8141(01)00035-9, 2001.
- 1109 Skarbek, R. M., A. W. Rempel, and D. A. Schmidt, Geologic heterogeneity can produce aseismic
1110 slip transients, *Geophys. Res. Lett.*, 39(21), L21306, doi:10.1029/2012GL053762, 2012.
- 1111 Song, T.-R. A., D. V. Helmberger, M. R. Brudzinski, R. W. Clayton, P. Davis, X. Perez-Campos,
1112 and S. K. Singh, Subducting slab ultra-slow velocity layer coincident with silent earthquakes in
1113 southern Mexico, *Science*, 324(5926), 502–506, doi:10.1126/science.1167595, 2009.
- 1114 Stefano, R. D., C. Chiariabba, L. Chiaryluce, M. Cocco, P. D. Gori, D. Piccinini, and L. Val-
1115 oroso, Fault zone properties affecting the rupture evolution of the 2009 (Mw 6.1) L’Aquila
1116 earthquake (central Italy): Insights from seismic tomography, *Geophys. Res. Lett.*, 38, L10310,
1117 doi:10.1029/2011GL047365, 2011.
- 1118 Sweet, J. R., K. C. Creager, and H. Houston, A family of repeating low-frequency earthquakes
1119 at the downdip edge of tremor and slip, *Geochem., Geophys., Geosyst.*, 15(9), 3713–3721, doi:
1120 10.1002/2014GC005449, 2014.

- 1121 Taira, T., D. S. Dreger, and R. M. Nadeau, Rupture process for micro-earthquakes inferred from
1122 borehole seismic recordings, *International Journal of Earth Sciences*, 104(6), 1499–1510, doi:
1123 10.1007/s00531-015-1217-8, 2015.
- 1124 Thomas, A. M., G. C. Beroza, and D. R. Shelly, Constraints on the source parameters of low-
1125 frequency earthquakes on the San Andreas Fault, *Geophys. Res. Lett.*, 43(4), 1464–1471, doi:
1126 10.1002/2015GL067173, 2016.
- 1127 Thomas, A. M., N. M. Beeler, Q. Bletery, R. Burgmann, and D. R. Shelly, Using low-frequency
1128 earthquake families on the San Andreas Fault as deep creepmeters, *J. Geophys. Res.*, 123(1),
1129 457–475, doi:10.1002/2017JB014404, 2018.
- 1130 Thomson, D. J., Spectrum estimation and harmonic analysis, *Proc. IEEE*, 70(9), 1055–1096, doi:
1131 10.1109/PROC.1982.12433, 1982.
- 1132 Tinti, E., E. Fukuyama, A. Piatanesi, and M. Cocco, A kinematic source-time function compatible
1133 with earthquake dynamics, *Bull. Seis. Soc. Amer.*, 95(4), 1211–1223, doi:10.1785/0120040177,
1134 2005.
- 1135 Uchide, T., P. M. Shearer, and K. Imanishi, Stress drop variations among small earthquakes before
1136 the 2011 Tohoku-oki, Japan, earthquake and implications for the main shock, *J. Geophys. Res.*,
1137 119(9), 7164–7174, doi:10.1002/2014JB010943, 2014.
- 1138 Ujiie, K., H. Saishu, Å. Fagereng, N. Nishiyama, M. Otsubo, H. Masuyama, and H. Kagi, An
1139 explanation of episodic tremor and slow slip constrained by crack-seal veins and viscous shear
1140 in subduction mélange, *Geophys. Res. Lett.*, 45, 5371–5379, doi:10.1029/2018GL078374, 2018.
- 1141 van Avendonk, H. J. A., W. S. Holbrook, D. Lizarralde, M. M. Mora, S. Harder, A. D. Bul-
1142 lock, G. E. Alvarado, and C. J. Ramírez, Seismic evidence for fluids in fault zones on top of
1143 the subducting Cocos Plate beneath Costa Rica, *Geophys. J. Intern.*, 181(2), 997–1016, doi:
1144 10.1111/j.1365-246X.2010.04552.x, 2010.
- 1145 Veedu, D. M., and S. Barbot, The Parkfield tremors reveal slow and fast ruptures on the same
1146 asperity, *Nature*, 532, 361–365, doi:10.1038/nature17190, 2016.
- 1147 Velasco, A. A., C. J. Ammon, and T. Lay, Empirical green function deconvolution of broadband
1148 surface waves: Rupture directivity of the 1992 Landers, California (Mw = 7.3), earthquake, *Bull.*
1149 *Seis. Soc. Amer.*, 84(3), 735–750, 1994.
- 1150 Venkataraman, A., and H. Kanamori, Observational constraints on the fracture energy of subduc-
1151 tion zone earthquakes, *J. Geophys. Res.*, 109(B5), B05302, doi:10.1029/2003JB002549, 2004.
- 1152 Veveakis, E., T. Poulet, and S. Alevizos, Thermo-poro-mechanics of chemically active
1153 creeping faults: 2. Transient considerations, *J. Geophys. Res.*, 119(6), 4583–4605, doi:
1154 10.1002/2013JB010071, 2014.
- 1155 Waldhauser, F., Near-real-time double-difference event location using long-term seismic archives,
1156 with application to northern California, *Bull. Seis. Soc. Amer.*, 99(5), 2736–2748, doi:
1157 10.1785/0120080294, 2009.

- 1158 Walter, J. I., S. Y. Schwartz, J. M. Protti, and V. Gonzalez, Persistent tremor within the northern
1159 Costa Rica seismogenic zone, *Geophys. Res. Lett.*, 38, L01307, doi:10.1029/2010GL045586,
1160 2011.
- 1161 Wang, E., and A. M. Rubin, Rupture directivity of microearthquakes on the San Andreas
1162 Fault from spectral ratio inversion, *Geophys. J. Intern.*, 186(2), 852–866, doi:10.1111/j.1365-
1163 246X.2011.05087.x, 2011.
- 1164 Watanabe, T., Y. Hiramatsu, and K. Obara, Scaling relationship between the duration and the
1165 amplitude of non-volcanic deep low-frequency tremors, *Geophys. Res. Lett.*, 34(7), L07305,
1166 doi:10.1029/2007GL029391, 2007.
- 1167 Webber, S., S. Ellis, and Å. Fagereng, “Virtual shear box” experiments of stress and slip
1168 cycling within a subduction interface mélange, *Earth Planet. Sci. Lett.*, 488, 27–35, doi:
1169 10.1016/j.epsl.2018.01.035, 2018.
- 1170 Wech, A. G., and K. C. Creager, Cascadia tremor polarization evidence for plate interface slip,
1171 *Geophys. Res. Lett.*, 34(22), doi:10.1029/2007GL031167, 2007.
- 1172 Yabe, S., and S. Ide, Spatial distribution of seismic energy rate of tectonic tremors in subduction
1173 zones, *J. Geophys. Res.*, 119(11), 8171–8185, doi:10.1002/2014JB011383, 2014.
- 1174 Yabe, S., and S. Ide, Slip-behavior transitions of a heterogeneous linear fault, *J. Geophys. Res.*,
1175 122(1), 387–410, doi:10.1002/2016JB013132, 2017.
- 1176 Yabe, S., A. S. Baltay, S. Ide, and G. C. Beroza, Seismic-wave attenuation determined from
1177 tectonic tremor in multiple subduction zonesseismic-wave attenuation determined from tec-
1178 tonic tremor in multiple subduction zones, *Bull. Seis. Soc. Amer.*, 104(4), 2043–2059, doi:
1179 10.1785/0120140032, 2014.
- 1180 Yang, H., Z. Li, Z. Peng, Y. Ben-Zion, and F. Vernon, Low-velocity zones along the San Jacinto
1181 Fault, Southern California, from body waves recorded in dense linear arrays, *J. Geophys. Res.*,
1182 119(12), 8976–8990, doi:10.1002/2014JB011548, 2014.
- 1183 Ye, L., T. Lay, H. Kanamori, and L. Rivera, Rupture characteristics of major and great (Mw $\zeta=$
1184 7.0) megathrust earthquakes from 1990 to 2015: 1. Source parameter scaling relationships, *J.*
1185 *Geophys. Res.*, 121(2), 826–844, doi:10.1002/2015JB012426, 2016.
- 1186 Zhang, J., P. Gerstoft, P. M. Shearer, H. Yao, J. E. Vidale, H. Houston, and A. Ghosh, Cascadia
1187 tremor spectra: Low corner frequencies and earthquake-like high-frequency falloff, *Geochem.,*
1188 *Geophys., Geosyst.*, 12(10), Q10007, doi:10.1029/2011GC003759, 2011.